

Gaia DR3 astrometric orbit determination with Markov Chain Monte Carlo and Genetic Algorithms

Systems with stellar, substellar, and planetary mass companions

B. Holl^{1,2,*}, A. Sozzetti³, J. Sahlmann⁴, P. Giacobbe³, D. Ségransan¹, N. Unger¹, J.-B. Delisle¹, D. Barbato^{1,3},
M.G. Lattanzi³, R. Morbidelli³, and D. Sosnowska¹

¹ Department of Astronomy, University of Geneva, Chemin Pegasi 51, CH-1290 Versoix, Switzerland

² Department of Astronomy, University of Geneva, Ch. d'Ecogia 16, CH-1290 Versoix, Switzerland

³ INAF - Osservatorio Astrofisico di Torino, Via Osservatorio 20, I- 10025 Pino Torinese, Italy

⁴ RHEA Group for the European Space Agency (ESA), European Space Astronomy Centre (ESAC),
Camino Bajo del Castillo s/n, 28692 Villanueva de la Cañada, Madrid, Spain

October 3, 2022

ABSTRACT

Context. Astrometric discovery of sub-stellar mass companions orbiting stars is exceedingly hard due to the required milliarcsecond precision, limiting the application of this technique to only a few instruments on a target-per-target basis as well as the global astrometry space missions Hipparcos and Gaia. The third Gaia data release (Gaia DR3) includes the first Gaia astrometric orbital solutions, whose sensitivity in terms of estimated companion mass extends down into the planetary-mass regime.

Aims. We present the contribution of the ‘exoplanet pipeline’ to the Gaia DR3 sample of astrometric orbital solutions by describing the methods used for fitting the orbits, the identification of significant solutions, and their validation. We then present an overview of the statistical properties of the solution parameters.

Methods. Using both a Markov Chain Monte Carlo and Genetic Algorithm we fit the 34 months of Gaia DR3 astrometric time series with a single Keplerian astrometric-orbit model that has 12 free parameters and an additional jitter term, and retain the solutions with the lowest χ^2 . Verification and validation steps are taken using significance tests, internal consistency checks using the Gaia radial velocity measurements (when available), as well as literature radial velocity and astrometric data, leading to a subset of candidates that are labelled as ‘validated’.

Results. We determined astrometric-orbit solutions for 1162 sources and 198 solutions have been assigned the ‘validated’ label. Precise companion mass estimates require external information and are presented elsewhere. To broadly categorise the different mass regimes in this paper we use the pseudo-companion mass \tilde{M}_c assuming a solar-mass host and define three solution groups: 17 (9 validated) solutions with companions in the planetary-mass regime ($\tilde{M}_c < 20 M_J$), 52 (29 validated) in the brown dwarf regime ($20 M_J \leq \tilde{M}_c \leq 120 M_J$), and 1093 (160 validated) in the low mass stellar companion regime ($\tilde{M}_c > 120 M_J$). From internal and external verification and validation we estimate the level of spurious/incorrect solutions in our sample to be of the order of $\sim 5\%$ and $\sim 10\%$ in the ‘OrbitalAlternative’ and ‘OrbitalTargetedSearch’ candidate sample, respectively.

Conclusions. We demonstrate that Gaia is able to confirm and sometimes refine known orbital companion orbits as well as identify new candidates, providing us with a positive outlook of the expected harvest from the full mission data in future data releases.

Key words. – astrometry – planets and satellites: detection – (stars:) brown dwarfs – (stars:) binaries: general – Catalogs – Techniques: radial velocities

1. Introduction

The third Gaia data release (Gaia DR3, Vallenari 2022) is the first release that includes non-single star (NSS) solutions (Gaia Collaboration et al. 2022; Pourbaix et al. 2022). The main astrometric NSS processing, which we will refer to as the ‘binary pipeline’, is described in Halbwachs et al. (2022). It analysed sources failing a single-star model using a cascade of double-star models of increasing complexity, up to the determination of a full orbital solution for one companion. An alternative NSS processing module being the subject of this paper, which we dub as the ‘exoplanet pipeline’, was designed with the two-fold goal of a) modeling higher-complexity NSS signals, such as those produced by multiple companions, and b) providing further insight

in the regime of low-amplitude signals, such as those produced by sub-stellar companions, i.e. exoplanets and brown dwarfs, around nearby stars. In Gaia DR3 we do not provide results for multiple companions due to the limited amount of available observations to constrain the solution. The per-source computational effort is higher for the exoplanet pipeline and the default channel for NSS processing is therefore the ‘binary pipeline’.

The design of the exoplanet pipeline takes advantage of some of the lessons learned from Doppler searches for planets. In particular, the modeling of complex, low-amplitude planetary signals can be prone to ambiguities in the interpretation of the results, with well-known cases in the recent literature of disagreement on the actual values of the orbital elements of a given companion, or on the number of companions, also depending on the details of the treatment of noise sources in the RV measurements.

* Corresponding author: B. Holl (berry.holl@unige.ch)

A non-exhaustive list of ‘controversies’ in radial velocity (RV) surveys includes the planetary systems around α Cen B (Dumusque et al. 2012; Hatzes 2013; Rajpaul et al. 2016), τ Ceti (Pepe et al. 2011; Tuomi et al. 2013; Feng et al. 2017a), GJ 667C (Anglada-Escudé et al. 2012, 2013; Delfosse et al. 2013; Feroz & Hobson 2014; Robertson & Mahadevan 2014), GJ 581 (Vogt et al. 2009; Baluev 2013; Robertson et al. 2014, 2015; Anglada Escudé & Tuomi 2015; Hatzes 2016; Trifonov et al. 2018), GJ 176 (Endl et al. 2008; Butler et al. 2009; Forveille et al. 2009), HD 41248 (Jenkins et al. 2013; Jenkins & Tuomi 2014; Santos et al. 2014; Feng et al. 2017b; Faria et al. 2019), Barnard’s Star (Ribas et al. 2018; Lubin et al. 2021), Kapteyn’s Star (Anglada Escudé et al. 2014; Robertson et al. 2015b; Anglada Escudé et al. 2016), GJ 3998 (Affer et al. 2016; Dodson-Robinson et al. 2022), Lalande 21185 (Butler et al. 2017; Diaz et al. 2019; Stock et al. 2020; Rosenthal et al. 2021; Hurt et al. 2022), BD -06° 1339 (Lo Curto et al. 2013; Simpson et al. 2022), and HD 219134 (Motalebi et al. 2015; Vogt et al. 2015; Gillon et al. 2017).

The above considerations prompted us to a methodological approach that implements two different algorithms for alternative orbit fitting of Gaia DR3 astrometry. The exoplanet pipeline was applied for processing of two datasets: the first contained a large number of sources for which none of the models attempted in the ‘binary pipeline’ could successfully improve upon the single-star fit based on the adopted thresholds on goodness-of-fit and significance statistics. These are labelled as either ‘OrbitalAlternative’ or ‘OrbitalAlternativeValidated’, with the union of the two sets labelled as ‘OrbitalAlternative[Validated]’ (or shorthand ‘OrbitalAlternative*’). The second constituted a much smaller collection of high-visibility sources, either because of their intrinsic nature, or because of already known sub-stellar and low-mass stellar companions around them. These are labelled as either ‘OrbitalTargetedSearch’ or ‘OrbitalTargetedSearchValidated’, with the union of the two sets labelled as ‘OrbitalTargetedSearch[Validated]’ (or shorthand ‘OrbitalTargetedSearch*’).

In this paper we provide an overview of the exoplanet pipeline, describe in details the functioning of the two orbit-fitting algorithms, and discuss the main characteristics of the orbital solution results obtained for the two processing experiments described above, which have been included in the Gaia DR3 archive of NSS solutions. It is important to point out that ‘Orbital’ solutions compatible with sub-stellar mass companions can also be found in the output of the ‘binary pipeline’ (cf. Halbwegs et al. 2022; Gaia Collaboration et al. 2022).

Our paper is organised as follows: in Sect 2 and 3 we shortly discuss the properties of the astrometric data and the model fitted to it. Section 4 describes the algorithms used to derive the orbital solutions and the procedure to select the best solutions. The input source selection and solution filtering procedures are detailed in Sect. 5, with result verification and validation in Sect. 6. We conclude in Sect. 7, with additional details regarding the reference solution data, acronyms list, and Gaia archive queries in Appendices A, C, and B, respectively.

2. Properties of the astrometric data

The input data spans about 34 months as shown in Fig. 1. It consists of time series of along-scan abscissa measurements w with respect to the reference position (α_0, δ_0) derived in the Gaia EDR3 Astrometric Global Iterative Solution (AGIS, see Lindgren et al. 2021) together with the associated scan angles and parallax factors. Details as well as several pre-processing steps are described in Halbwegs et al. (2022) and section 7.2.2

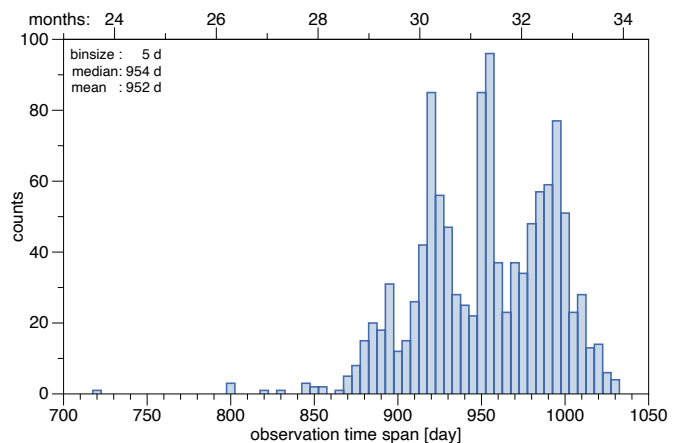


Fig. 1. Histogram of the observation time spans.

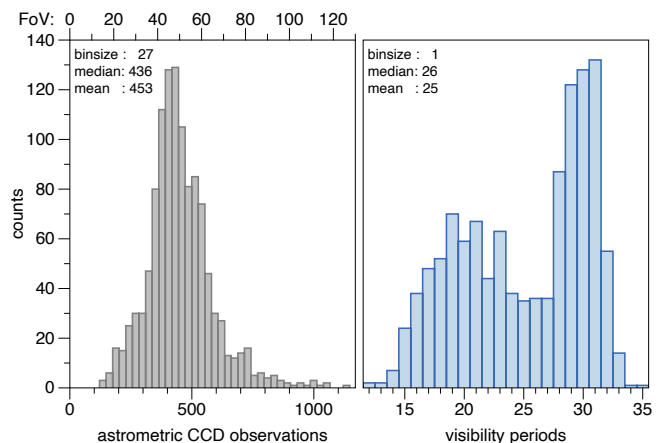


Fig. 2. Histogram of number of CCD observations and visibility periods. The number of CCD observations is divided by nine to provide the approximate number of FoV observations above the left panel.

of the DR3 NSS documentation (Pourbaix et al. 2022) which include per-FoV¹ CCD outlier rejection and modification of the measurements of stars with $\varpi > 5$ mas (i.e., within 200 pc) to take into account the perspective acceleration (to identify the latter see `f1ags` in Sect. 3.3). Figure 2 shows the number of observations per source after outlier rejection. As expected the minimum number of visibility periods² is not less than about 13, i.e., the number of parameters we are solving for with a single Keplerian orbit. Fitting for a second orbit would require an additional 7 parameters and thus (at least) 20 visibility periods. For this and various other reasons the general attempt to fit for more than one Keplerian was not made for Gaia DR3.

The mean and median of the per-CCD uncertainties of each source are shown in Fig. 3. The outlier rejection applied in the ‘binary pipeline’ pre-processing step did not remove all strong outliers in abscissa value and/or uncertainty, which generally is the reason for the difference between the mean and median. In the orbit figures that we show later (Figs. 13 - 14), the persist-

¹ One field-of-view (FoV) passage of a source across the Gaia focal plane generally produces 8 or 9 individual CCD transits, each corresponding to the passage of the source image across an astrometric-field (AF) detector (Gaia Collaboration et al. 2016).

² A ‘visibility period’ groups observations separated from other groups by at least 4 days which (usually) assures that scan-angle and parallax factors have changed by a significant amount due to the evolution of the scanning law, and therefore is a better measure of independent ‘epochs’ than simply counting CCD observations or FoV transits.

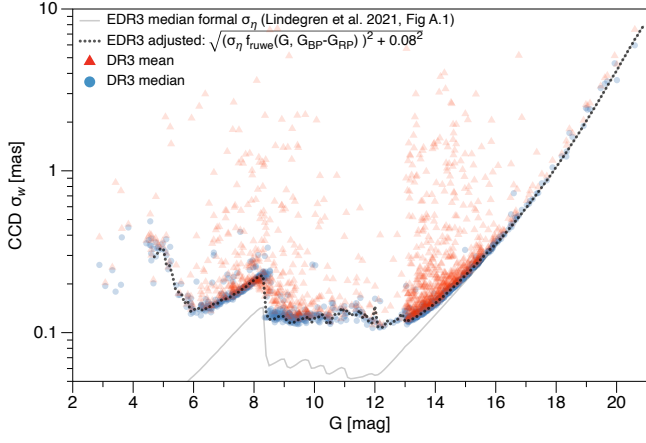


Fig. 3. Mean and median CCD AL-scan abscissa uncertainty σ_w per source.

ing outliers are usually not displayed. We compare these data with the EDR3 median formal uncertainty σ_η of Lindegren et al. (2021) (their fig. A.1 red median line), here drawn as grey line. For the estimation of the CCD AL-scan abscissa uncertainty σ_w in the astrometric NSS pipeline, the σ_η was first inflated by³ $f_{ruwe}(G, G_{BP} - G_{RP})$, after which a (typical value of) 0.08 mas calibration noise was added in quadrature. The result is shown as the dotted line in Fig. 3, nicely matching the lower envelope of the median σ_w of our sources.

However, the abscissa data used for Gaia DR3 is generally affected by some level of under/over estimation of uncertainties and potential biases, which can lead to unrealistic good or bad goodness-of-fit statistics. To mitigate the effects of such undefined noise contributions we fitted for an additional jitter term similar to the AGIS `astrometric_excess_noise`, as explained in Sect. 3. In fact, it proved difficult to define general filtering criteria to distinguish spurious and significant solution. This task required additional procedures where many sources were individually checked against literature data (in this release leading to those labelled ‘validated’), see Section 6.

3. Astrometric model

3.1. Mathematical description

As discussed in Sect. 2, the input data for the exoplanet pipeline are the Gaia along-scan abscissa measurements w . For a binary system and neglecting all noise considerations, these can be modelled by the combination of a single-source model w_{ss} , describing the standard astrometric motion of the system’s barycentre, and a Keplerian model w_{k1} .

The single-source model can be written as

$$w_{ss} = (\Delta\alpha^* + \mu_{\alpha^*} t) \sin \psi + (\Delta\delta + \mu_\delta t) \cos \psi + \varpi f_\varpi, \quad (1)$$

where $\Delta\alpha^* = \Delta\alpha \cos \delta$ and $\Delta\delta$ are small offsets in equatorial coordinates from some fixed reference point (α_0, δ_0) , μ_{α^*} and μ_δ are proper motions in these coordinates, t is time since reference time J2016.0, ϖ is the parallax, f_ϖ is the parallax factor, and ψ is the scan angle. The Gaia scan angle is defined as having a value of $\psi = 0$ when the field-of-view is moving towards local North,

³ The renormalisation function value that transforms the AGIS unit weight error (uwe) into renormalised unit weight error (ruwe), see for details the definition of the Gaia archive `ruwe` parameter.

and $\psi = 90^\circ$ towards local East⁴. This is not the same convention as used for Hipparcos (e.g. F. van Leeuwen 2007).

The astrometric motion corresponding to a Keplerian orbit of a binary system has generally seven independent parameters. These are the period P , the epoch of periastron passage T_0 , the eccentricity e , the inclination i , the ascending node Ω , the argument of periastron ω , and the semi-major axis of the photocentre a_0 . The Thiele-Innes coefficients A, B, F, G , which linearise part of the equations are defined as:

$$A = a_0 (\cos \omega \cos \Omega - \sin \omega \sin \Omega \cos i) \quad (2)$$

$$B = a_0 (\cos \omega \sin \Omega + \sin \omega \cos \Omega \cos i) \quad (3)$$

$$F = -a_0 (\sin \omega \cos \Omega + \cos \omega \sin \Omega \cos i) \quad (4)$$

$$G = -a_0 (\sin \omega \sin \Omega - \cos \omega \cos \Omega \cos i) \quad (5)$$

The elliptical rectangular coordinates X and Y are functions of eccentric anomaly E and eccentricity:

$$E - e \sin E = \frac{2\pi}{P}(t - T_0) \quad (6)$$

$$X = \cos E - e \quad (7)$$

$$Y = \sqrt{1 - e^2} \sin E \quad (8)$$

The single Keplerian model can then be written as

$$w_{k1} = (B X + G Y) \sin \psi + (A X + F Y) \cos \psi. \quad (9)$$

The combined model $w^{(\text{model})}$ for the Gaia along-scan abscissa is

$$\begin{aligned} w^{(\text{model})} &= w_{ss} + w_{k1} \\ &= (\Delta\alpha^* + \mu_{\alpha^*} t) \sin \psi + (\Delta\delta + \mu_\delta t) \cos \psi + \varpi f_\varpi \\ &\quad + (B X + G Y) \sin \psi + (A X + F Y) \cos \psi. \end{aligned} \quad (10)$$

This model has been extensively used for modelling the Hipparcos epoch data of non-single stars (e.g. Sahlmann et al. 2011a).

More details on the modelling of non-single star data in the Gaia pipelines can be found in the DR3 NSS documentation Pourbaix et al. (2022) and in Halbwachs et al. (2022), where in the latter the instantaneous scan angle is described as the coordinate-derivative of the abscissa, e.g. $\sin \psi = \frac{\partial w}{\partial \Delta\alpha^*}$.

Finally, to account for potentially unmodelled signals or modelling errors, we additionally fit for a jitter term which is added in quadrature to the provided uncertainties of the along-scan abscissa, bringing the total number of fitted parameters to 13: five linear parameters for the single-source model w_{ss} , seven for the single Keplerian model w_{k1} (of which the four A, B, F, G are linear), and one non-linear jitter term σ_{jit} .

Symmetric parameter uncertainty estimates are obtained by reconstructing the covariance matrix directly from the Jacobians of all parameters for all observations. No scaling of these formal covariances was performed, which might potentially suffer from over/under estimations e.g. due to unmodelled signals (that might be partially absorbed by the jitter term).

⁴ <https://www.cosmos.esa.int/web/gaia/scanning-law-pointings>

3.2. Conversion of Thiele-Innes parameters to Campbell elements

The conversion of the Thiele-Innes parameters (A, B, F, G) to Campbell or geometric elements (a_0, ω, Ω, i) is in principle straight-forward (e.g. Halbwegs et al. 2022) but several caveats exist that are related to the amplitudes of the A, B, F, G covariance terms which sometimes seem to be over-estimated, in particular for solutions with poorly-constrained eccentricities (cf. Gaia Collaboration et al. 2022; Babusiaux et al. 2022). In Sect. 6.1.6 we discuss some examples. Unless specifically mentioned, all figures with Campbell element values in this paper use the linear error propagation. Regarding the semi-major axis, in this work we always assume the companion is sufficiently non-luminous that the semi-major axis of the photocentre and that of the observed host star are the same, i.e., $a_1 = a_0$, and will only refer to a_1 .

3.3. Archive model parameter fields

Table 1 provides an overview of all solution parameters and additional fields populated for our sources in the `nss_two_body_orbit` Gaia DR3 archive table.

The `goodness_of_fit` is the F2, or so-called ‘gaussianized chi-square’ (Wilson & Hilferty 1931), which should approximately follow a normal distribution with zero mean value and unit standard deviation for good fits.

The `flags` field only has integer values 0, 64, and 192. Value 0 translates to no bit-flags being set. Value 64 translates to bit 6 being set: which means that a mean RV value was available, and value 192 translates to bit 6 and 7 being set, where bit 7 indicates that mean RV was used for perspective acceleration correction of the local plane coordinates. In our published sample there are 164 sources with flags value 0, 571 sources with flags value 64, and 427 sources with flags value 192 (see result of query provided in Appendix B for finer details).

The `astrometric_n_obs_al` provides the number of CCD observations that were available before outlier rejection. In the archive the `astrometric_n_good_obs_al` should represent the number after outlier rejection, but erroneously ended up to report the same value as `astrometric_n_obs_al`. Figure 2 shows the correct number of filtered (‘good’) observations. For completeness we document here that the number of rejected CCD observations varies between zero and 269, with the majority having zero to three observations rejected, and the vast majority less than 12 observations rejected.

We did not make use of the `efficiency` parameter in our verification, which incidentally is 0 for a large fraction of our sample.

Gaia photometric time series are available for 76 sources in our sample, i.e., sources in `gaia_source` with `has_epoch_photometry=true`. Of these, 75 overlap with the variable source catalogue (Eyer et al. 2022) and one source (367906215676634752) was released as part of the Gaia Andromeda Photometric Survey (Evans et al. 2022), which can be identified in `gaia_source` by `phot_variable_flag=VARIABLE` and `in_andromeda_survery=true`, respectively. In this Gaia DR3 no Gaia astrometric time series were made public.

4. Processing procedure

Astrometric orbit modelling requires solving a highly non-linear least squares problem with a minimum of 12 parameters

Table 1. `gaia_dr3.nss_two_body_orbit` table fields filled for the 1162 sources from the exoplanet pipeline described in this paper. Parameter names link directly to the online data model documentation.

Gaia DR3 table field name	unit	symbol	notes
<code>solution_id</code>			
<code>source_id</code>			
<code>nss_solution_type</code>			four types ^a
<code>ra</code>	deg	α_*	
<code>ra_error</code>	mas	σ_{α_*}	
<code>dec</code>	deg	δ	
<code>dec_error</code>	mas	σ_{δ}	
<code>parallax</code>	mas	ϖ	
<code>parallax_error</code>	mas	σ_{ϖ}	
<code>pmra</code>	mas/yr	μ_{α_*}	
<code>pmra_error</code>	mas/yr	$\sigma_{\mu_{\alpha_*}}$	
<code>pmdec</code>	mas/yr	μ_{δ}	
<code>pmdec_error</code>	mas/yr	$\sigma_{\mu_{\delta}}$	
<code>a_thiele_innes</code>	mas	A	
<code>a_thiele_innes_error</code>	mas	σ_A	
<code>b_thiele_innes</code>	mas	B	
<code>b_thiele_innes_error</code>	mas	σ_B	
<code>f_thiele_innes</code>	mas	F	
<code>f_thiele_innes_error</code>	mas	σ_F	
<code>g_thiele_innes</code>	mas	G	
<code>g_thiele_innes_error</code>	mas	σ_G	
<code>period</code>	d	P	
<code>period_error</code>	d	σ_P	
<code>t_periastron</code>	d	T_0	since J2016.0
<code>t_periastron_error</code>	d	σ_{T_0}	
<code>eccentricity</code>		e	
<code>eccentricity_error</code>		σ_e	
<code>astrometric_n_obs_al</code>			
<code>astrometric_n_good_obs_al</code>			
<code>bit_index</code>			8191 ^b
<code>corr_vec</code>			^c
<code>obj_func</code>		χ^2	
<code>goodness_of_fit</code>		F2	
<code>efficiency</code>			{0, [0.26–0.44]}
<code>significance</code>		a_1/σ_{a_1}	
<code>flags</code>			{0, 64, 192}
<code>astrometric_jitter</code>	mas	σ_{jit}	

Notes. ^(a) The four types we described: ‘OrbitalAlternative[Validated]’ and ‘OrbitalTargetedSearch[Validated]’ ^(b) Always value 8191, i.e. in bits flagging the 12 orbital parameters (excluding `astrometric_jitter`) ^(c) vector form of the upper triangle of the correlation matrix (column-major ordered) of the 12 solved parameters (excluding `astrometric_jitter`).

(Sect. 3). The orbital motion is usually seen as a small perturbation of the standard stellar motion, with a magnitude that can be orders of magnitude smaller than those of parallax and proper motion. This motivated the original design of the ‘exoplanet’-element of the non-single-star (NSS) processing pipeline (see DR3 NSS documentation Pourbaix et al. (2022) for the full NSS pipeline structure). In particular, it was recognised that orbit modelling in the limit of low signal amplitudes would benefit from a more in-depth (computationally expensive) parameter search, which translated in the adoption of two independent orbit fitting algorithms exploiting different philosophies, which are described in turn below. Both algorithms are executed in parallel, and a standard recipe based on Bayesian model selection is utilised to select the best-fit solution, as further detailed below.

4.1. Differential Evolution Markov Chain Monte Carlo

The first orbit fitting code is a hybrid implementation of a Bayesian analysis based on the differential evolution Markov chain Monte Carlo (DE-MCMC) method (Ter Braak 2006; East-

man et al. 2013). An earlier version of the code had been extensively tested in Casertano et al. (2008), while its upgrade has been recently used in Drimmel et al. (2021). In this scheme we take advantage of the four (A , B , F , G) Thiele-Innes constants representation (see Sect. 3.1. See also e.g., Binnendijk 1960; Wright & Howard 2009) to partially linearize the problem. Within this dimensionality reduction scheme, only three non-linear orbital parameters must be effectively explored using the DE-MCMC algorithm (e.g., Casertano et al. 2008; Wright & Howard 2009; Mendez et al. 2017; Drimmel et al. 2021), namely P , T_0 , and e . The fourth model parameter explored the DE-MCMC way is an uncorrelated astrometric jitter term σ_{jit} . At each step of the DE-MCMC analysis, the resulting linear system of equations is solved in terms of the Thiele-Innes constants using simple matrix algebra, QR decomposition being the method of choice. The final likelihood function used in the DE-MCMC analysis is then:

$$-\ln(\mathcal{L}) = \frac{1}{2} \sum_{j=1}^{N_{\text{astr}}} \frac{(w_j^{(\text{obs})} - w_j^{(\text{model})})^2}{\sigma_{w,j}^2 + \sigma_{\text{jit}}^2} + \frac{1}{2} \sum_{j=1}^{N_{\text{astr}}} \ln(\sigma_{w,j}^2 + \sigma_{\text{jit}}^2) \quad (11)$$

The DE-MCMC analysis is carried out with a number of chains equal to twice the number of free parameters. A period search is first performed in order to identify statistically more probable periodicities. Given the nature of the astrometric dataset, the direct application of publicly available tools for the periodogram analysis of unevenly sampled time-series (e.g. the Generalized Lomb-Scargle periodogram, Zechmeister & Kürster 2009) is not possible. For any given source, the DE-MCMC module draws a large sample of initial trial periods for sinusoidal signals projected along the scan directions of the time-series, based on a uniform grid up to twice the observations time span. A sparsely sampled selection of periods corresponding to local χ^2 minima becomes the seed for the P parameter initialization of the DE-MCMC chains. Uniform priors in the ranges $[-P/2, P/2]$ and $[0, 10]$ mas are used for T_0 and σ_{jit} , respectively. Finally, starting values for e are drawn from a Beta distribution, following Kipping (2013).

Convergence and good mixing of the chains are checked based on the Gelman–Rubin statistics (e.g., Ford 2006). The medians of posterior distributions are taken as the final parameters. In order to comply with the choice of the main non-single-star processing chain (Halbwachs et al. 2022), we did not adopt the standard approach for computing the 1σ uncertainties on model parameters, i.e. evaluating the ± 34.13 per cent intervals from the posterior distributions, which typically results in asymmetric error-bars, but rather provided symmetric estimates of the uncertainties by reconstructing the covariance matrix directly from the Jacobians of all parameters for all observations.

4.2. Genetic Algorithm

The implementation of the Genetic Algorithm for Gaia (MIKS-GA) is a direct adaptation of YORBIT, a tool used to search for exoplanets in radial velocity time series (Ségransan et al. 2011; Hébrard et al. 2016; Triaud et al. 2017; Kiefer et al. 2019; Triaud et al. 2022a). An implementation of the MIKS-GA algorithm has been successfully used to discover brown-dwarf binaries from the orbital solutions identified in high-precision astromet-

ric timeseries obtained with ground-based telescopes (Sahlmann et al. 2013, 2015a, 2020).

Genetic Algorithms (GA) are a class of optimization algorithms that are loosely based of Darwin’s theory of evolution by natural selection (Holland 1975; Jong 1988). In GA, a population of chromosomes is initialised and evolves by applying a set of genetic operators (such as crossover, recombination, mutation and selection) until the best genotype dominates the population. Such algorithms are particularly well suited for highly non-linear model with irregular sampling provided that the genetic operators are fine-tuned to the specificity of the problem.

Here, a chromosome consists of the non-linear parameters needed to model a merit function \mathcal{M} defined as the sum of the log-likelihood and the log-prior. We further assume that the residuals of the astrometric data to the model are drawn from independent realisations of a Normal distribution of zero mean with a variance composed of the astrometric uncertainty plus an additional jitter term which accounts for anything in the data that can’t be modelled by the analytical astrometric model. It results in the following expression of the merit function

$$\mathcal{M}(\{t, \psi, w, \sigma_w\}; \{P, e, M_0, \sigma_{\text{jit}}\}) = -\ln(\mathcal{L}) - \ln(\mathcal{P}) \quad (12)$$

and the log-likelihood :

$$-\ln(\mathcal{L}) = \frac{1}{2} \sum_{j=1}^{N_{\text{astr}}} \frac{(w_j^{(\text{obs})} - w_j^{(\text{model})})^2}{\sigma_{w,j}^2 + \sigma_{\text{jit}}^2} + \frac{1}{2} \sum_{j=1}^{N_{\text{astr}}} \ln(\sigma_{w,j}^2 + \sigma_{\text{jit}}^2) + \frac{N_{\text{astr}}}{2} \ln(2\pi) \quad (13)$$

The priors expression is the product of uniform distributions for the mean anomaly M_0 computed at J2016.0 (JD 2457388.5) in Gaia DR3, for the frequency (between 2.5 d and two times the observation time span), for the log of the jitter term (between $[0.005, 2\sigma_{5p,\text{res}}]$ mas, where $\sigma_{5p,\text{res}}$ is the standard deviation of the residuals of a 5-parameter astrometric fit to the observations), and of a truncated normal distribution for the eccentricity (with $\mu = 0$, $\sigma = 0.3$, truncated over $[0, 0.985]$) to penalise highly eccentric orbit solutions that commonly arise in low Signal-to-Noise time series with irregular sampling.

$$\mathcal{P} = \mathcal{T} \mathcal{N}_e(0, 0.3, 0, 0.985) \cdot U_f(\nu_{\min}, \nu_{\max}) \cdot U_{M_0}(0, 360) \cdot U_{\sigma_{\text{jit}}}(-2.30, \log(2\sigma_{5p,\text{res}})) \quad (14)$$

4.2.1. Initialisation phase

The initialisation phase of the chromosomes’ population is based on a frequency analysis of the Gaia astrometric time series and on the analytical determination of orbital elements using Fourier analysis (Delisle & Ségransan 2022). To do so, a least-square periodogram (Lomb 1976; Scargle 1982) of the Gaia astrometric time series is built (Delisle & Ségransan (2022), see Eq. 15), comparing for each frequency, the *chi-square* of a circular orbit model plus the parallactic motion (χ_{9p}^2) to the *chi-square* of the parallactic motion only (χ_{5p}^2).

$$z_{\text{GLS}}(\nu) = \frac{\chi_{5p}^2 - \chi_{9p}^2(\nu)}{\chi_{5p}^2} \quad (15)$$

The first step consists in drawing a set of frequencies from a log-uniform law $\log(\mathcal{V}) \sim U(\log(\nu_{\min}), \log(\nu_{\max,\text{init}}))$ (between

2.5 d and the observation time span), where frequencies with a lower significance according to the SDE statistic (Signal Detection Efficiency, see Alcock et al. 2000; Kovács et al. 2002) are redrawn until selected. This procedure discards from the initial population, periodic signals with lower probability, improving the efficiency of the GA.

The second step of the initialisation concerns the eccentricity and the mean anomaly. For 50% of the chromosomes, the eccentricity is drawn according to $\sqrt{e} \sim U(0, \sqrt{0.985})$ while the mean anomaly is uniformly drawn according to $M_0 \sim U(0, 2\pi)$. For the remaining 50% of the chromosomes, the eccentricity and the mean anomaly are analytically derived using the signal frequency decomposition described in Delisle & Ségransan (2022) and drawn accordingly to $N(\hat{e}, \sigma_{\hat{e}})$ and $N(\hat{M}_0, \sigma_{\hat{M}_0})$. Finally, the astrometric jitter σ_{jit} of each chromosome is drawn from a log-uniform distribution $\log(\Sigma_0) \sim U(\log(0.005 \text{ mas}), \log(2\sigma_{5p,\text{res}}))$.

The last stage of the initialisation phase of the GA consists in evaluating the merit function \mathcal{M} of each chromosome in the population.

4.2.2. Evolution

The evolution of the population is done by randomly drawing chromosomes from the population and by applying to them genetic operators. The efficiency of the GA is improved by applying the genetic operators on the non-linear parameters of the model only while the linear parameters are obtained through a linear regression.

Drawing Process : The first step consists in drawing a local random sub-population of 5x5 to maximum 7x7 chromosomes (from the 80x80 full population) over which several operators are applied, among which these four are especially effective :

- Full Crossover : Two chromosomes (mother & father) are drawn from the sub-population from which a child genome is bred with the frequency, mean anomaly, eccentricity and astrometric jitter randomly drawn from the mother & father. The child chromosomes replaces the worst chromosomes in a local sub-population according to the merit function.
- Harmony Mutation : A chromosome is randomly drawn from the sub-population and a new frequency is drawn among possible harmonics. The mutated chromosome replaces the worst chromosome in a local sub-population according to the merit function. This operator is efficient to find the period of eccentric orbits where the fundamental frequency is not always dominant.
- Alias Mutation : A chromosome is randomly drawn from the sub-population and a new frequency is randomly drawn from the aliases spectral window frequencies. The mutated chromosome replaces the worst chromosome in a local sub-population according to the merit function. This operator is efficient to find the true fundamental frequency of unevenly sampled data.
- Simplex Mutation : The best chromosome is selected from the sub-population and is improved using a Nelder-Mead Simplex algorithm and replaces the worst chromosome in a local sub-population according to the merit function. This operator is efficient at the end of the evolution and allows to reach convergence towards the best merit function.

The computation time allocated to each genetic operator depends on its ability to improve the merit function at different stages of evolution. In order to avoid the population converging to a local maximum, a minimum computation time is assigned to all operators.

4.2.3. Termination

Termination is reached once 95 % of the population has converged towards the maximum merit function or that the total computing time reaches 60 seconds.

4.3. Pipeline execution and best solution choice

The sequential pipeline execution of the DE-MCMC and GA orbit fitting modules is as follows:

1. both modules are executed independently, until convergence is achieved on an optimized best-fit configuration or for a maximum execution time of 60 sec. Each algorithm produces the best-fit parameter solution based on their internal likelihood merit functions: Eq. 11 for DE-MCMC and Eq. 13 for GA;
2. when both modules have obtained convergence, the selection of the statistically preferred solution is made based on the Bayesian Information Criterion (BIC, Schwarz 1978): $\text{BIC} = k \ln(n) - 2 \ln \mathcal{L}$ (where k is the number of parameters estimated by the model and n is the number of data points). The adopted best-fit model is the one with the lowest BIC. It is published if it passes the subsequent export filters (see Sect. 5). No information is published on which module provided a particular source solution. For the Gaia DR3 processing the GA always provided the maximum likelihood while the DE-MCMC provided the more conservative median of its posterior distribution around the best solution. This imbalanced solution comparison led to the vast majority of published solutions to be provided by GA; something we intend to improve upon in Gaia DR4.

5. Source selection and solution filtering

5.1. Stochastic solutions: ‘OrbitalAlternative’

5.1.1. Input source list

The Gaia non-single-star (NSS) processing pipeline tests out a variety of astrometric solution models (Halbwachs et al. 2022; Pourbaix et al. 2022) and if none fits the data to a satisfactory degree the single-star solution from Gaia EDR3 was retained, in which the excess noise will have absorbed any unmodelled (presumably ‘stochastic’) signal. Though the exoplanet pipeline is too computationally intensive to be run on all sources that pass through the NSS chain (see Sect. 4), it is however run on this sample of 2,457,530 presumed stochastic sources to look for difficult to detect orbital signals with both the DE-MCMC and GA algorithms. This sample is mostly composed of faint and distant sources.

5.1.2. Solution filtering

Force-fitting the sample of sources that had received a stochastic solution returned a vast majority of solutions of dubious quality, primarily due to known aliasing effects with scanning law periodicities (Holl et al. 2022). An aggressive filtering strategy was

therefore applied to the output of the exoplanet pipeline in order to provide a sub-sample of candidate solutions for which the likelihood of retaining spurious solutions would be minimized. We filtered solutions utilizing the following constraints:

- fractional difference in parallax between the one fitted by the exoplanet pipeline and that in the original EDR3 single-star solution $< 5\%$;
- statistical significance of the derived semi-major axis of the orbit $a_1/\sigma_{a_1} > 20$ (uncertainty derived from the Thiele-Innes parameters using linear error propagation);
- ratio of the EDR3 astrometric excess noise to the uncorrelated jitter term fitted by the exoplanet pipeline > 20 ;
- number of individual FoV transits > 36 ;
- EDR3 parallax of the source > 0.1 mas.

Overall, the sample that survived the filtering process is composed of 629 orbital solutions. The selected solutions have a period distribution mostly free of the doubtful spurious values as discussed in Sect. 6.2.4. The filtered sample is published in Gaia DR3 with the `nss_solution_type` ‘OrbitalAlternative[Validated]’, and it underwent careful inspection for verification and validation purposes, as described in Sect. 6).

5.2. Input source list: ‘OrbitalTargetedSearch’

5.2.1. Input source list

The modules of the exoplanet pipeline have been in development from a time before the launch of Gaia and were verified mostly with the help of simulated data. Only from DR3 the number of epochs and calibration noise-level were sufficient to fit meaningful orbits with the exoplanet pipeline. In order to test its performance with real data we compiled source lists that would serve the following purposes:

- Pipeline testing, verification, and validation, e.g. for demonstrating that the orbits of known exoplanets can be detected.
- Sample the properties of Gaia astrometric time-series in different regimes, e.g. bright and faint, and investigate how that influences pipeline performance.

As we progressed in understanding the performances of the non-single star pipelines and when the input source selection for the binary pipeline was finalised (Halbwachs et al. 2022), it was decided to perform a dedicated (additional) run of the exoplanet pipeline on a pre-defined source list, hence the orbital name suffix ‘OrbitalTargetedSearch’.

Starting from the previously defined list of test sources, we therefore compiled a more extensive sample for the targeted search. We identified sources for which information on the presence/absence of exoplanets and substellar companions was available in the literature, typically these were stars included in observational planet-search programs. The list included:

- Sources in the Nasa Exoplanet Archive⁵. These are hosts of confirmed and candidate exoplanets discovered with various observation techniques.
- Sources in planet-search programmes, predominantly using spectrographs for precision radial-velocity measurements. This included the samples of e.g. HIRES (Butler et al. 2017), CORALIE (Udry et al. 2000), HARPS (Mayor et al. 2003), SOPHIE (Bouchy et al. 2009), and HARPS M-dwarfs (Bonfils et al. 2013).

⁵ <https://exoplanets.nasa.gov/discovery/exoplanet-catalog/>

- Sources in known astrometric binaries from the Hipparcos binary solutions compiled in Table F1 of F. van Leeuwen (2007).

All the source samples above consist predominantly of bright stars ($G \lesssim 10$). We complemented these with sources that promised compelling scientific outcomes in the case of orbit detection, and that may otherwise have not been processed with an orbit-fitting pipeline. For example, the binary pipeline only processed sources with $G < 19$, regardless of distance. To probe fainter sources that yet remain within a distance horizon that in principle allows the detection of signals caused by sub-stellar companions, we included the ultra-cool dwarf sample of Smart et al. (2019) and metal-polluted white dwarfs within 20 pc from the Sion et al. (2014) and Giammichele et al. (2012) compilations. The total number of unique sources selected for the targeted search was 19 845.

We obtained Gaia DR2 source identifiers of these targets either directly from the respective catalog, from Simbad (Wenger et al. 2000), or from a positional crossmatch with the Gaia DR2 catalog. The corresponding Gaia DR3 identifiers were then submitted for the dedicated processing run.

5.2.2. Solution filtering

In-depth scrutiny of the resulting solutions was performed on multiple levels, in an attempt to retain the most sensible orbits. The different steps taken in order to filter out implausible solutions, which we detail below, have an important degree of heterogeneity, and our final choices translate in a complex selection function.

Our approach to solution filtering was three-fold. We first defined various indicators of the statistical significance of the solutions, then we fine-tuned their threshold values with an iterative process, and lastly performed a selection of different sub-samples of solutions based on different choices of subsets of the indicators. The statistical filters included an extensive model comparison with alternative, less-complex models to safeguard detection of bona-fide candidates, distance-dependent threshold for the orbit significance, relative agreement between the fitted parallax and the AGIS parallax, an upper limit to the derived value of the mass function, a constraint on closed orbits, and variable thresholds for the value of the ratio of the AGIS astrometric excess noise to the Keplerian jitter term in the solution.

We used two sets of statistical filters, in each set the filters were applied in conjunction and then the full list was constructed with the targets that passed the filters of either one OR the other set.

Set 1:

- $\text{BIC}_{\text{Kep}} - \text{BIC}_5 < -30$
- $\text{BIC}_{\text{Kep}} - \text{BIC}_7 < -30$
- $\varpi > \sigma_{\text{jit}}$
- $|\Delta\varpi| < 0.5 a_1$
- $a_1/\sigma_{a_1} > 2$
- $P < \Delta T$
- $f(M) < 0.02$
- $\sigma_{\text{jit}} < \max(0.1, 2\sigma_{\text{jit,agis}})$
- $\sigma_{\text{STD}} < 1.5\sigma_{\text{MAD}}$

Set 2:

- $|\Delta\varpi| < 0.05 \varpi$
- $a_1/\sigma_{a_1} > 5$
- $\sigma_{\text{jit,agis}}/\sigma_{\text{jit}} > 5$

where BIC_{Kep} is the BIC for the Keplerian solution, and BIC_5 and BIC_7 are the BIC for the 5 and 7 parameter solution respectively⁶. ϖ is the parallax from the Keplerian solution, $|\Delta\varpi|$ is the absolute difference between the parallax of the Keplerian solution and the AGIS parallax, a_1 and σ_{a_1} are respectively the semi-major axis and its uncertainty, P is the period of the companion, ΔT is the time span of observation for each target, $f(\mathcal{M})$ is the mass function of the primary/companion system and is calculated as $f(\mathcal{M}) = v^2 a_1^3 / G$ (where $v = 2\pi/P$, is the orbital frequency), σ_{jit} is the astrometric excess noise as calculated by the exoplanet pipeline, $\sigma_{jit,agis}$ is the astrometric excess noise from the 5-parameter AGIS solution, σ_{STD} is the weighted standard deviation of the residuals of the Keplerian solution, and σ_{MAD} is 1.4826 times the Median Absolute Deviation (MAD) of the residuals of the Keplerian solution.

We complemented the statistical filtering approach with visual inspection of individual orbits (see Sect 6.2.2). In this way we looked for symptoms of spurious results due to e.g. important numbers of outliers and/or correlated residuals even for cases of statistically robust solutions. Finally, we used a threshold (10%) in the relative agreement between the fitted value of P and that from existing literature data and independent Gaia solutions as additional discriminant, in an attempt to recover bona-fide solutions that otherwise might have been discarded based on too-stringent statistical filtering. The final number of sources with solutions accepted for publications in Gaia DR3 is 533, of which 188 were validated with the `nss_solution_type` ‘OrbitalTargetedSearchValidated’ (see Sect. 6.3).

The difficulties we faced in converging on a coherent approach for the identification of well-defined classes of robust solutions and spurious orbits are illustrative of the challenges inherent in the Gaia DR3 NSS processing, particularly in the limit of low astrometric SNR (and correspondingly low companion mass) for bright stars, which are still affected by limitations in the error model, as well as the generally low number of visibility periods (see Sect. 2). We caution users against performing detailed statistical analyses with this sample of orbital solutions.

6. Results

In total the exoplanet pipeline populates 1162 orbits in the Gaia DR3 table `nss_two_body_orbit` into four `nss_solution_type`: ‘OrbitalAlternative’ (619), ‘OrbitalAlternativeValidated’ (10), ‘OrbitalTargetedSearch’ (345), and ‘OrbitalTargetedSearchValidated’ (188).

Calibrated companion mass estimates require additional non-astrometric information and thus are out of the scope of this paper; they are presented in Gaia Collaboration et al. (2022).

To ease the interpretation of the ‘OrbitalAlternative[Validated]’ and ‘OrbitalTargetedSearch[Validated]’ sub-sample figures, they are always shown side by side: the former on the left and the latter on the right. For brevity we will in the text below refer to these two categories as ‘OrbitalAlternative*’ and ‘OrbitalTargetedSearch*’ to refer to the union sample of the non-validated and validated solutions in both categories.

6.1. General overview

6.1.1. Sky distribution

The sky distribution of our solutions is shown in Fig. 4. Clearly the filtering on ‘OrbitalAlternative*’ has selected sources in regions of the sky with sufficiently dense sampling, causing ‘holes’ mainly around low ecliptic latitudes ($|\beta| < 45^\circ$) that are generally less well sampled. In contrast, the external input catalog-based ‘OrbitalTargetedSearch*’ has a much more uniform distribution.

6.1.2. Signal to noise estimate

In Fig. 5 we explore the approximate signal-to-noise ratio of our results, where the fitted semi-major axis (a_1 [mas]) is taken as a proxy for the signal level, and the median abscissa uncertainty as the noise proxy. We compare two commonly used definitions: the top panels show that of Casertano et al. (2008) with its typical proposed threshold of 3, and the bottom panel shows that of Sahlmann et al. (2015b) with its proposed threshold of 20. Only three (0.3 %; two validated) solutions fall below the Sahlmann et al. (2015b) threshold, whereas 515 (44 %; 33 validated) solutions fall below the Casertano et al. (2008) threshold.

We see that the majority of our sample has reasonable to high signal to noise, though targets having very low signal to noise levels generally are the least massive companions, as expected.

On the ordinate axis we plot the significance of the derived semi-major axis (a_1/σ_{a_1}), which shows the expected trend that higher signal to noise is associated with better constrained parameter estimates.

6.1.3. Goodness-of-fit statistics

In Fig. 6 we present the goodness-of-fit statistics that are available in the Gaia data archive (Sect. 3.3): χ^2 (`obj_func`) and F2 (`goodness_of_fit`). While the former is difficult to interpret globally without compensating for the varying number of degrees of freedom (i.e. the χ^2_{red}), the latter F2, ‘gaussianized chi-square’, is expected to follow a normal distribution with zero mean and unit standard deviation, as shown with the thin green line. Comparison to the histogram and a fit to it (thick black line) shows that the distribution is not completely symmetric but generally is rather well-behaved. This can however largely be subscribed to the inclusion of the non-linear jitter term σ_{jit} model parameter (see Sect. 3.1 and Figs. 9 and 17) which was meant to absorb any unmodelled variance in the data, and thus likely contributed to the ‘normalisation’ of the expected goodness-of-fit statistics.

6.1.4. Parameter distributions

Starting with Fig. 7, we see in the top row panels that the period eccentricity is well constrained by a 5-day circularisation period (formulation of Halbwachs et al. 2005) and that our validated targets generally have medium to low eccentricities. Due to the aggressive filtering on the ‘OrbitalAlternative*’ mainly periods above 100 d and orbits with eccentricities below 0.4 were selected.

The second row right panel show that the different pseudo-mass groups roughly follow a $a_1 \propto P^{2/3}$ relation with different offsets, which is what one would expect from Kepler’s third law for the astrometric signal of systems with similar distance and

⁶ Ranalli et al. (2018) presents an independent approach of using BIC for model selection.

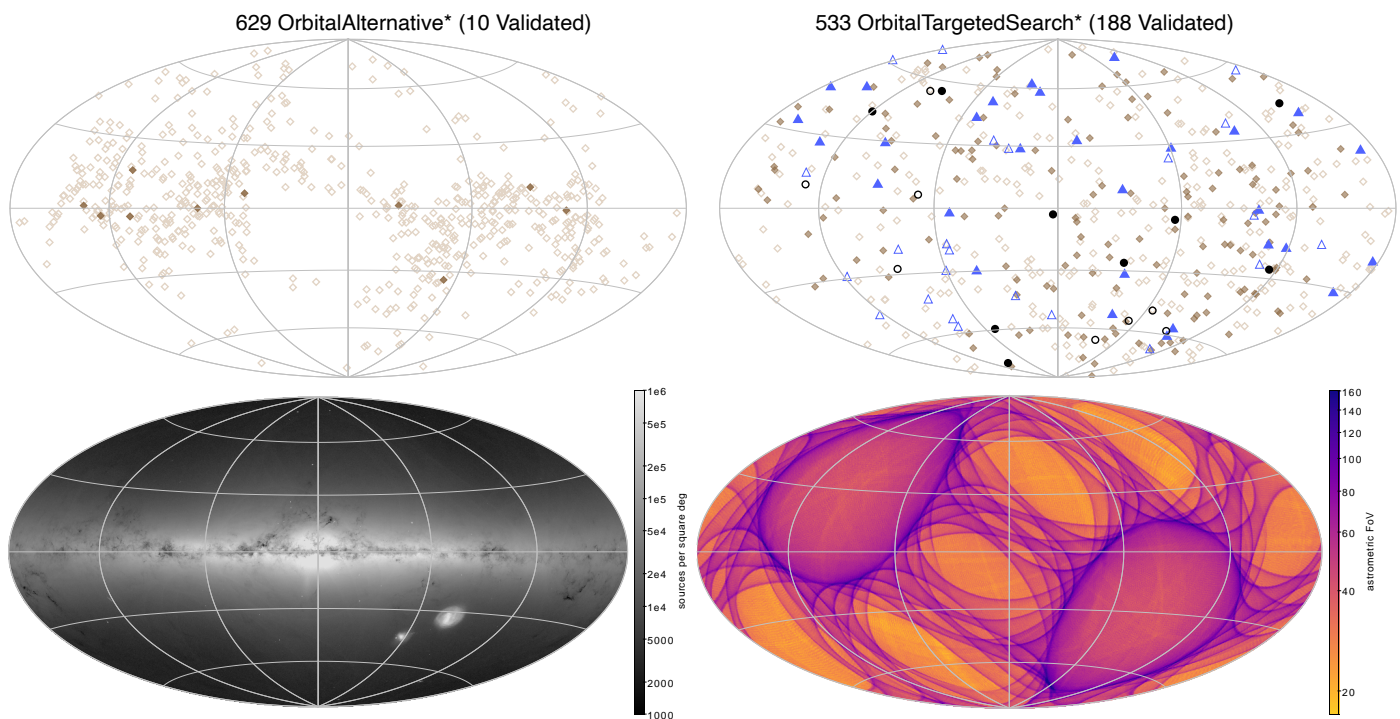


Fig. 4. Galactic sky distribution of our published solutions, longitude increasing to the left. We broadly categorise the different mass regimes using the pseudo-companion mass \tilde{M}_c assuming a solar-mass host and define three solution groups: 17 (9 validated) solutions with companions in the planetary-mass regime ($\tilde{M}_c < 20 M_J$, black circles), 52 (29 validated) in the brown dwarf regime ($20 M_J \leq \tilde{M}_c \leq 120 M_J$, blue triangles), and 1093 (160 validated) in the low mass stellar companion regime ($\tilde{M}_c > 120 M_J$, orange diamonds). Validated targets are plotted as (dark) filled symbols, while open symbols are used for the non-validated targets. Same symbols are used in Fig. 5 and following figures. Top left panel: ‘OrbitalAlternative*’; top right panel: ‘OrbitalTargetedSearch*’; bottom left panel: Gaia DR3 source sky density; bottom right panel: (maximum) number of DR3 astrometric FoV transits.

mass (ratio) companions. Looking at the third row right panel we see that indeed the sources are roughly at a typical distance of about 50 pc. In the left panel we see that the distance distribution is rather widely spread out and thus would not produce a nice relation in the period versus a_1 plot above it. Note the excess of high semi-major axis solution for short periods in the left plot: these are likely spurious or incorrect period detections (see Gaia Collaboration et al. 2022).

The third row panels also illustrate that the ‘blind search’ ‘OrbitalAlternative*’ sample (left) is at much fainter magnitudes and larger distances than the ‘OrbitalTargetedSearch*’ (right), the latter being largely compiled from radial velocity literature sources thus not surprisingly consisting of mostly relatively bright targets.

The fourth row of panels show the zero-extinction absolute magnitude estimate, based on parallax and G-band apparent magnitude, see discussion in Sect. 6.2.1 for more details.

Note that both the discussed parallax-based ‘distance’ and absolute magnitude estimates are meaningful given that the uncertainty on the parallax is generally (much) smaller than 20% of the value, see bottom panel of Fig. 8. This is further supported by the relatively ‘tightness’ of the HR diagram in the bottom right panel.

Figure 9 presents us with several parameters as function of a_1 . We start with the jitter term, which for most ‘OrbitalAlternative*’ is around or below an insignificant 0.01 mas. For the ‘OrbitalTargetedSearch*’ the level is generally around 0.1 mas, and for about a dozen the jitter level is above $a_1/2$, i.e., an (unmodelled) noise of the same order as the orbital solution semi-major axis.

The second row of panels shows the significance of the semi-major axis (a_1/σ_{a_1}), which is around 20-30 for the ‘OrbitalAlternative*’ sample and spans several orders of magnitude for the ‘OrbitalTargetedSearch*’ sample. As expected, in both cases the validated samples generally have a relatively high significance.

The cosine inclination distribution on the third row of panels is rather flat for the ‘OrbitalAlternative*’ as expected for random oriented systems. For the ‘OrbitalTargetedSearch*’ we see an excess of edge-on systems, as expected given that the input selection was mainly based on radial velocity targets. The bottom two rows show the longitude of the ascending node (Ω) and periastron argument (ω) which both are relatively flat for both samples, as expected for randomly-oriented orbits. A general discussion of the expected distributions and observed biases in the geometric orbital elements of astrometric orbits is given in Gaia Collaboration et al. (2022).

6.1.5. Parameter uncertainties

We systematically inspect the parameter uncertainties of all fitted parameters versus their value and do not see any unexpected trends or outliers. As noted in Sect. 3.1, we exported the formal uncertainties as provided from the covariance matrix of the best-solution least-squares solution, without any scaling. As we know from the astrometric jitter term that there is some level of unmodelled noise left in the data, these values might not always give reliable estimates of the true uncertainties of these parameters. See also Sect. 3.2 related to propagation of uncertainties on derived parameters.

For a few interesting parameters we plot the data shown in Fig. 8: the top panels show the period uncertainty versus pe-

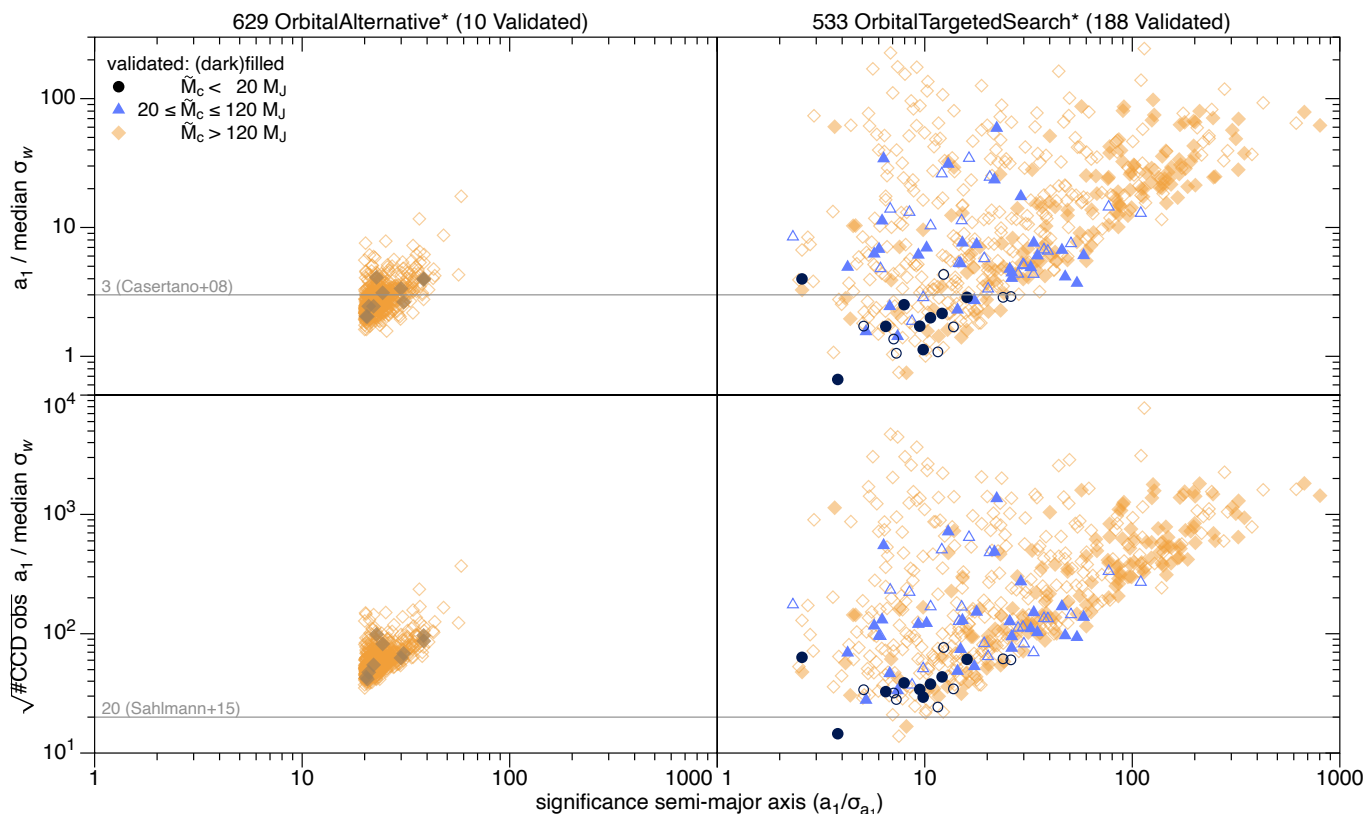


Fig. 5. Signal to noise ratio of a_1 with respect to the median abscissa uncertainty. Top panel: statistic used in Casertano et al. (2008) with its typical proposed threshold of 3, bottom panel: statistic used in Sahlmann et al. (2015b) with its proposed threshold of 20.

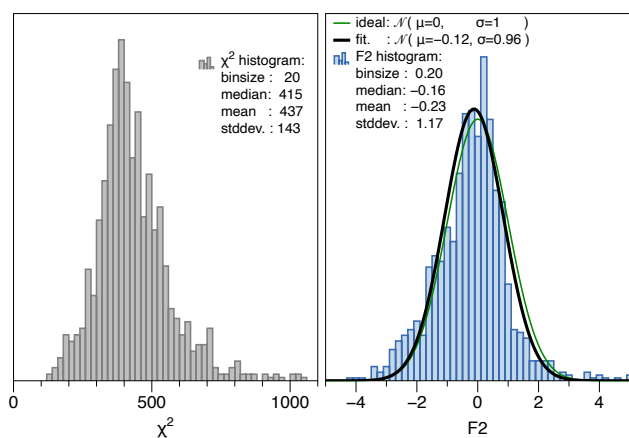


Fig. 6. Goodness of fit statistics. Left panel: χ^2 (obj_func in Table 1); right panel: F2 (goodness_of_fit in Table 1).

riod along with an observation time span (i.e. cycle-normalised) phase shift of 5%, below which almost all solutions lie, except for the longest periods as expected due to the mild constraints on the period due to the very low cycle count.

The second row of panels show the eccentricity uncertainty versus their value, which is typically between 0.06 – 0.1 for the ‘OrbitalAlternative*’, but varies over a much wider range for the ‘OrbitalTargetedSearch*’, though the majority of the latter still remains below a meaningful uncertainty of 0.2.

The epoch periastron has been distributed between -0.5 – 0.5 of the period around T_0 as shown in the third row of panels, and is rather flatly distributed in this range, as expected. A relative

uncertainty above 1 (solid line) clearly is non-informative, which luckily only happens for a dozen of objects in either category.

Finally, we show also the relative parallax uncertainty in the bottom row of panels, which shows that the majority of our sample has relative precision better than 5%, and almost all better than 10%. Given that 20% is an absolute minimum to use parallaxes as distance estimator, we are confident that the distance and absolute magnitude estimates in the bottom two panel rows of Fig. 7 are meaningful.

6.1.6. Campbell element estimation

Figures 10 and 11 show the differences between using Monte-Carlo resampling or linear propagation for calculating values and uncertainties of these geometric parameters and their significance. Generally there is good agreement, but for about ten solutions the Monte-Carlo estimate for the semimajor axis is much larger than the linearly-estimated one. These cases typically correspond to solutions with poorly-constrained eccentricities (i.e. $e/\sigma_e < 1$) for which Monte Carlo resampling is not recommended because of unrealistic variances of the Thiele-Innes coefficients (Babusiaux et al. 2022). This is also reflected in the comparison of the semimajor significance estimators (Fig. 11), which shows significant discrepancies predominantly for solutions with poorly-constrained eccentricities.

There are four solutions with linearly-propagated ω -uncertainties $\sigma_\omega > 1000$ deg and those also have small or very small eccentricities. Therefore both Monte Carlo resampling and linear propagation can lead to unrealistic results for some almost-circular orbits.

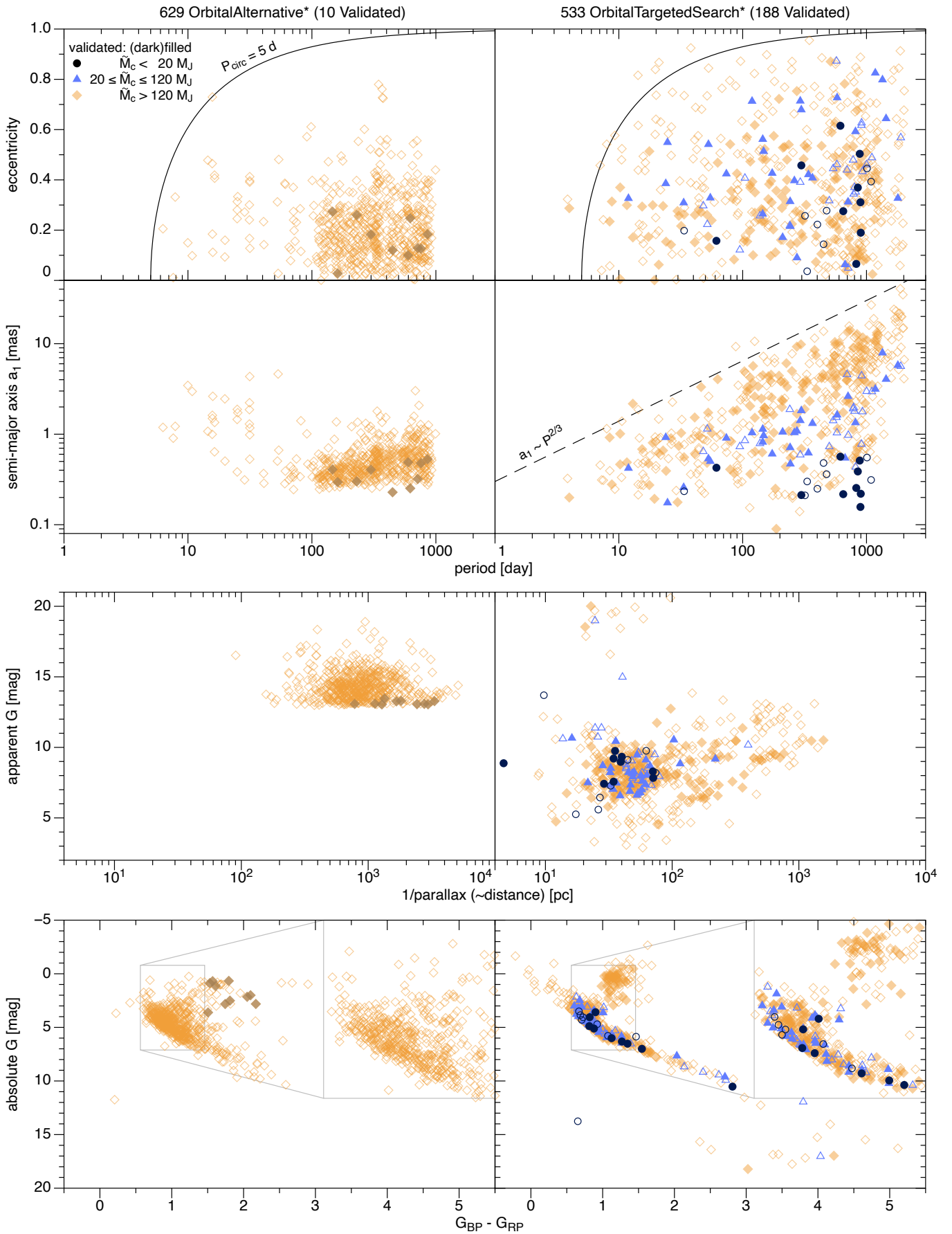


Fig. 7. Parameter distributions of the published solutions: period-eccentricity and period versus semi-major axis (top panels), apparent magnitude versus inverse parallax (third panel), zero-extinction absolute magnitude versus colour (bottom panel). See Sect. 6.1.4 and 6.2 for discussion.

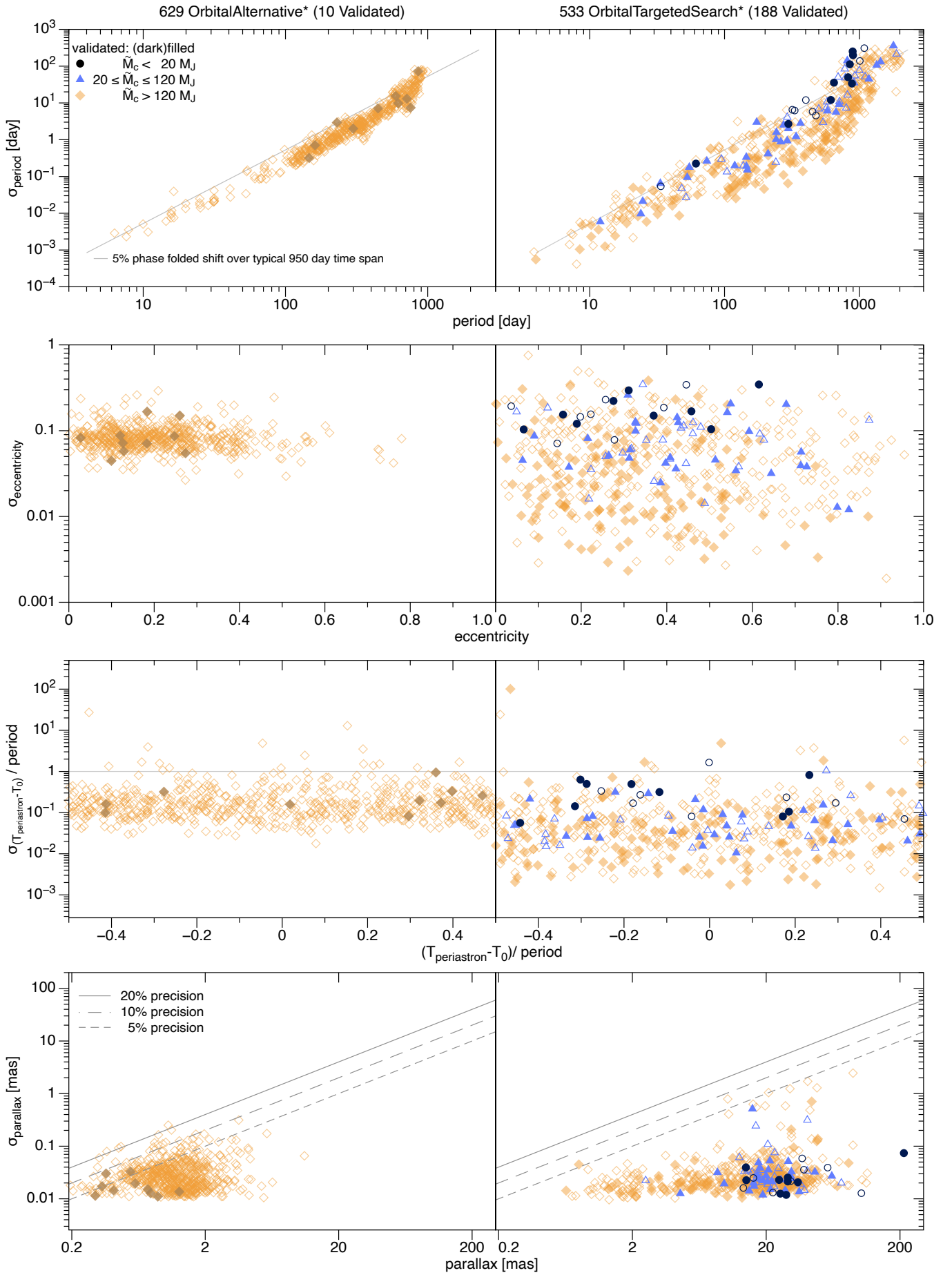


Fig. 8. Uncertainties for period (top panel), eccentricity (second panel), periastron epoch (third panel), and parallax (fourth panel) as function of the parameter value itself. See Sect. 6.1.5 for discussion.

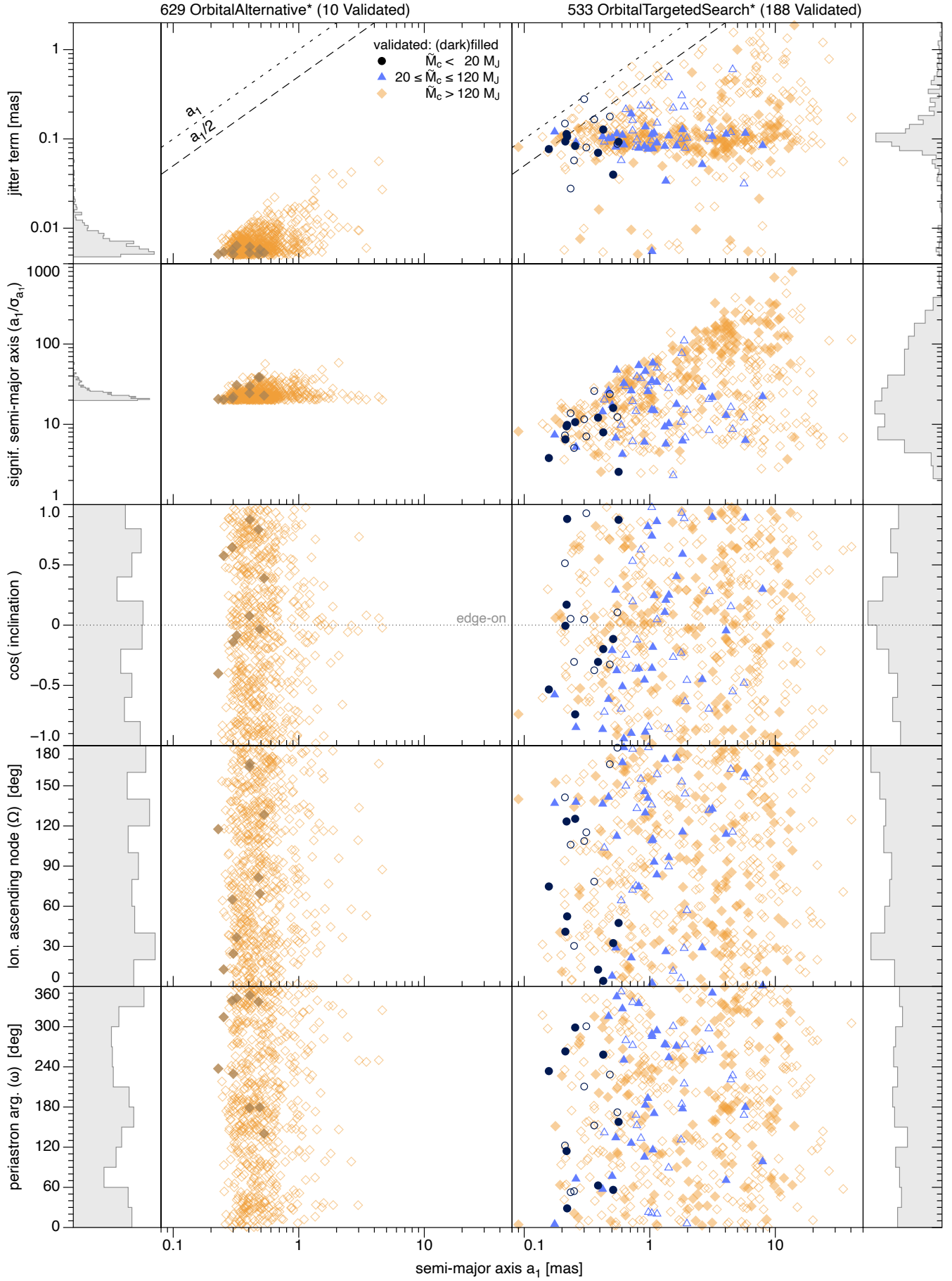


Fig. 9. Parameter distributions as function of (photocentre) semi-major axis a_1 : jitter term (top panel), semi-major axis (second panel), cosine of the inclination (third panel), longitude of the ascending node (fourth panel), and periastron argument (bottom panel). See Sect. 6.1.4 for discussion.

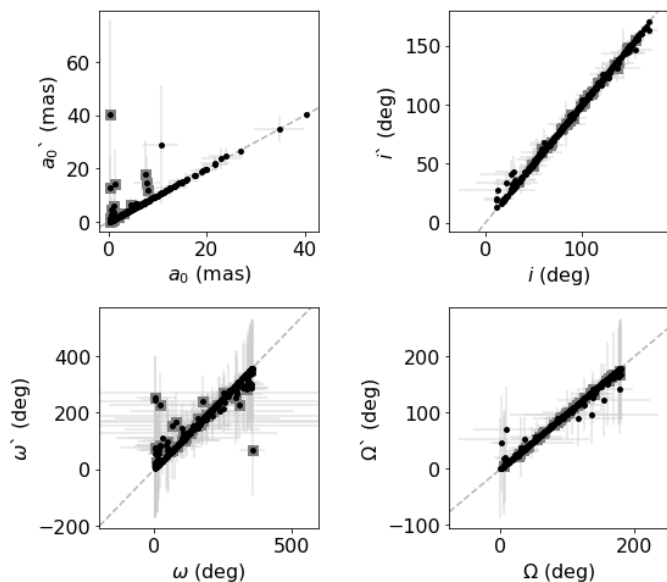


Fig. 10. Values and uncertainties for geometric elements. Estimates using linear error propagation and Monte-carlo resampling are shown on the x- and y-axes respectively. In the latter case, the median value is adopted with a symmetric uncertainty computed as the mean of the upper and lower 1- σ -equivalent confidence interval. The dashed line indicates equality and solutions with $e/\sigma_e < 1$ are marked with grey squares. Large discrepancies in ω at the $360^\circ \rightarrow 0^\circ$ boundary (e.g., the point on the bottom right) are of no major concern.

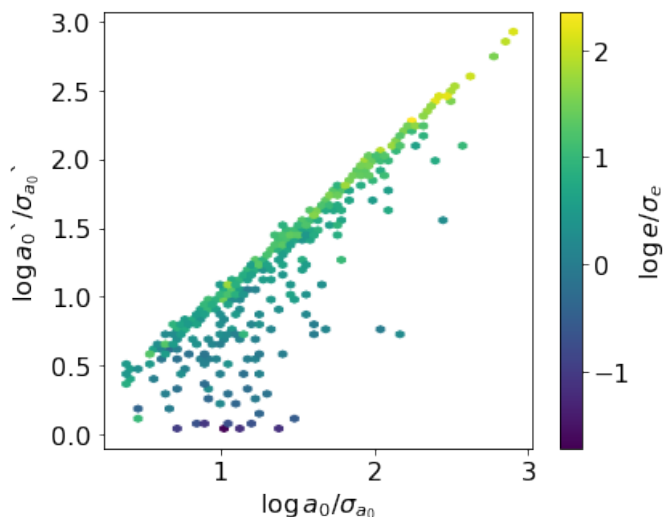


Fig. 11. Significance estimates (a over σ_a). Density histogram of estimates using linear error propagation and Monte-carlo resampling on the x- and y-axis, respectively. The histogram bins are colour-coded by the average eccentricity significance e/σ_e .

6.2. Verification

In this verification section the focus is on confirming bona fide companions based on internal consistency checks and expectations.

6.2.1. HR-diagram position

The bottom row of panels in Fig. 7 shows the zero-extinction absolute magnitude estimate (i.e. $G_{\text{apparent}} + 5(\log 10(\varpi/1000) + 1)$, with ϖ in [mas]). Most of our host-stars lie along the main sequence, though a small fraction are likely (sub-)giants. Interestingly, all ‘OrbitalAlternativeValidated’ sources (i.e., the filled

dark orange diamonds) appear to belong to the latter class. The relative tightness of the HR diagram in the right panel reinforces the correctness of our parallaxes having high relative precision, and that extinction amongst most of these targets is likely low. A binary sequence is not clearly identifiable (in contrast to fig. 47 of Gaia Collaboration et al. 2022), which further reinforces the expectation that the sample is not significantly polluted by ‘impostors’ masquerading as systems with small-mass ratios and negligible flux ratios but that are instead binaries with a flux ratio close to the mass ratio.

6.2.2. Astrometric orbit visualisation

We generated graphical representations of all ‘OrbitalTargeted-Search*’ solutions. These contain the modelled astrometric motion, the post-fit residuals, and auxiliary information describing the properties of the source’s data and fit-quality metrics. These figures were used as an empirical tool to assess the quality of the solutions, but not to validate them. The visual discovery of a doubtful solution usually led to the identification or refinement of filter criteria. In other words, this visual inspection was most efficiently used for identifying spurious solutions that should be rejected.

Figures 12 – 16 show examples of orbit visualisations, which were obtained on the basis of the `pystrometry` package (Sahlmann 2019)⁷. An additional example which also demonstrated the solution validation with external RVs is the case of HD 81040, which was showcased in a Gaia Image of the Week (https://www.cosmos.esa.int/web/gaia/iow_20220131).

These figures illustrate the different regimes in terms of sampling, source magnitude, measurement uncertainty, and orbit size in which our algorithms were successful in identifying significant solutions. The scientific implications of the shown orbital solutions are discussed in Gaia Collaboration et al. (2022).

6.2.3. Comparison with AGIS solution excess noise

A crude, but generally effective indicator of improved modelling is to compare the excess noise level between the 5-parameter AGIS solution and Keplerian orbit solution (called jitter term in the latter). The top panels of Fig. 17 show that for the most massive companions we have more than an order of magnitude decrease in the residuals noise level, though for the less massive companions this difference is reduced, as expected.

The second row of panels shows an interesting relation between the AGIS excess noise and fitted semi-major axis: typically the semi-major axis is about half the AGIS excess noise, which holds true for the wide range of masses and semi-major axis in our sample. Comparison of other parameters with those from AGIS do not present any unexpected deviations and are not shown.

6.2.4. Spurious orbits

Figure 18 shows an example of the period-eccentricity diagram from the unfiltered stochastic solution sample. The clear structure of period aliases corresponding to e.g. 1 year, 6 months, the 63-days precession period of the satellite, and their harmonics is further discussed in Holl et al. (2022). The green filled dots correspond to P and e values from ‘OrbitalAlternative’ solutions equivalent to the data in the top left panel of Fig. 7. Note that

⁷ <https://github.com/Johannes-Sahlmann/pystrometry>

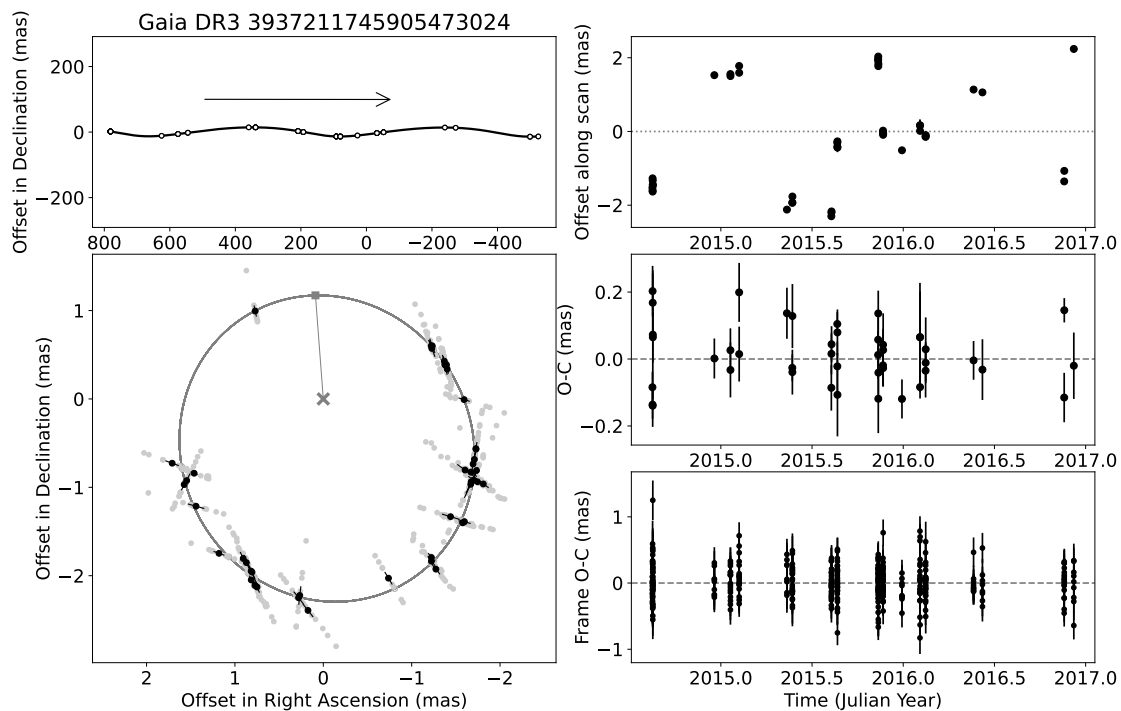


Fig. 12. Astrometric orbit of HD 114762 i.e. Gaia DR3 3937211745905473024 (left bottom panel) as determined by Gaia ($G = 7.15$ mag, $P = 83.74 \pm 0.12$ day, $e = 0.32 \pm 0.04$, $\varpi = 25.36 \pm 0.04$ mas). North is up and East is left. The sky-projected orbit model about the system barycentre marked with an "x" is shown in grey and astrometric measurements and normal-points after subtraction of parallax and proper motion are shown in grey and black, respectively. Only one-dimensional ("along-scan") astrometry was used, therefore the shown offsets are projected along Gaia's instantaneous scan angle, whose orientation is also indicated by the error-bars. The star's modelled parallax and proper motion is shown in the top-left panel by the solid curve, where open circles indicate the times when the star crossed the Gaia field-of-view. The arrow indicates the direction of motion. The top-right panel shows the normal points after subtraction of the parallax and proper motion as a function of time. The middle-right and bottom-right panel shows the post-fit residual normal-points and individual CCD-transit data, respectively. Normal-points are computed at every field-of-view transit of the star from the ~ 9 individual CCD transits and are only used for visualisation, whereas the data processing uses individual CCD-transit data.

these large number of spurious solutions were mostly filtered out by our aggressive filter criteria described in Sect. 5, at the cost of removing potentially good solution and thus overall low completeness.

The adopted solution filtering procedure did not include constraints on the mass function. A few percent of unrealistically large values of $f(M)$ primarily with short orbital periods ($P \lesssim 100$ days) is still present. As further discussed in Gaia Collaboration et al. (2022), these are likely to be spurious, and therefore the level of contamination of the 'OrbitalAlternative' solutions is probably around 5%. In Gaia Collaboration et al. (2022) (see Sect. 5.1) a recipe is provided for effectively excluding such spurious orbits based on constraints of the parallax significance as a function of the orbital period of the solution.

The identification of likely spurious solutions in the 'OrbitalTargetedSearch' sample, and corresponding estimate of the degree of contamination, was performed as part of the validation analysis, and is described in the following sections.

6.3. Validation

Validation includes comparison with available literature radial velocity or astrometry data, as well as Gaia radial velocity solutions. These were used to grant certain candidate orbits the status of 'Validated', identified by this suffix to their `nss_solution_type`.

6.3.1. Literature astrometric solutions

In the 'OrbitalTargetedSearch' category, literature astrometric orbits for two targets were available: DE0823-49 (Gaia DR3 5514929155583865216, Sahlmann et al. 2013) and 2M0805+48 (Gaia DR3 933054951834436352, Sahlmann et al. 2020) both being consistent with the Gaia orbit and thus leading to their 'Validated' suffix. They are listed in Appendix A.

6.3.2. Literature radial velocity solutions

When available, literature radial velocity data was used to vet the full subset of candidate companions with $\tilde{M}_c < 120 M_J$ (i.e., assuming $1 M_\odot$ host) and a subset with $\tilde{M}_c > 120 M_J$ in the 'OrbitalTargetedSearch' candidate set. When the orbital parameters (typically the period and eccentricity) between the RV solution and the Gaia solution were found to be consistent, it resulted in the 'Validated' suffix, all of which are listed in Appendix A.

For several sources the RV reference parameters are not given, this is to indicate that the RV data alone was not enough to validate the orbit on its own (e.g. there were multiple significant peaks in the RV periodogram). In those cases we validated the target if the RV data was consistent after constraining the period of the keplerian to the Gaia orbital period.

If no literature RV solution was found the source was kept without additional suffix in the name, i.e., it stayed a candidate. When an astrometric orbit was found to be incompatible with

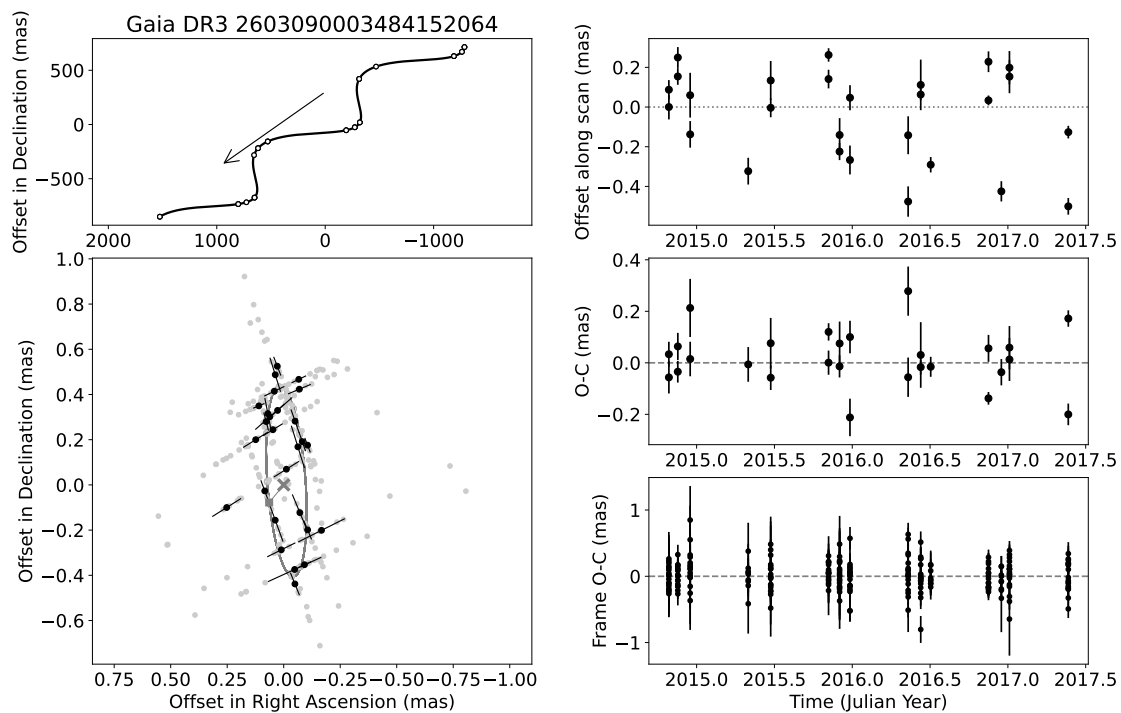


Fig. 13. Same as Fig. 12 but for Gl 876 i.e. Gaia DR3 2603090003484152064 ($G = 8.88$ mag, $P = 61.36 \pm 0.22$ day, $e = 0.16 \pm 0.15$, $\varpi = 213.79 \pm 0.07$ mas).

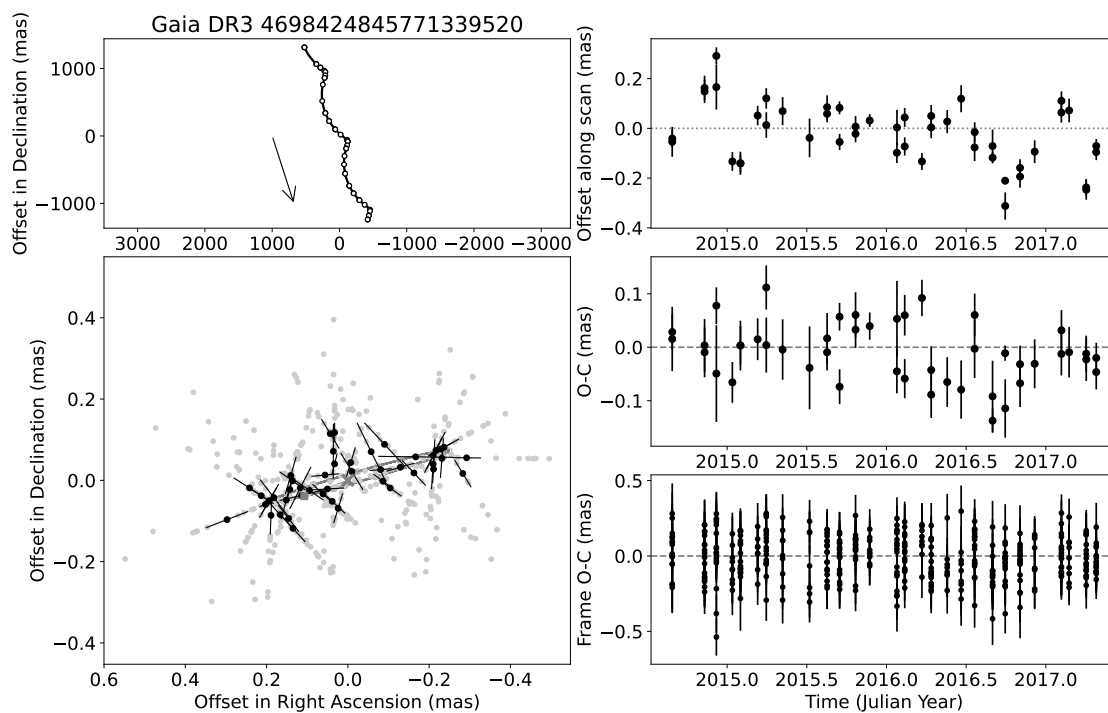


Fig. 14. Same as Fig. 12 but for WD0141-279 i.e. Gaia DR3 4698424845771339520 ($G = 13.70$ mag, $P = 33.65 \pm 0.05$ day, $e = 0.20 \pm 0.15$, $\varpi = 102.87 \pm 0.01$ mas).

RV data it was removed from our publication list, thus making this validation step part of the filtering process (see Sect. 5.2.2).

While this step of the validation procedures was performed quite carefully, it is not entirely free from pitfalls. For example, a small number of sources with good matches between the fitted and literature P values were not flagged as 'Validated', and are still listed in Table A.2 with solution type 'OrbitalTargetedSearch'. These include two known RV planet hosts, HR

810 (Gaia DR3 4745373133284418816) and HD 142 (Gaia DR3 4976894960284258048), as well as

Gaia DR3 2133476355197071616 (Kepler-16 AB). The latter source hosts the first circumbinary planet detected by the *Kepler* mission, with $P = 105$ d (Doyle et al. 2011; Triaud et al. 2022b). In this case Gaia detects a companion with $P = 41$ d and an almost edge-on orbit, which is in fact the low-mass stellar companion Kepler 16 B eclipsing Kepler-16 A. In a few

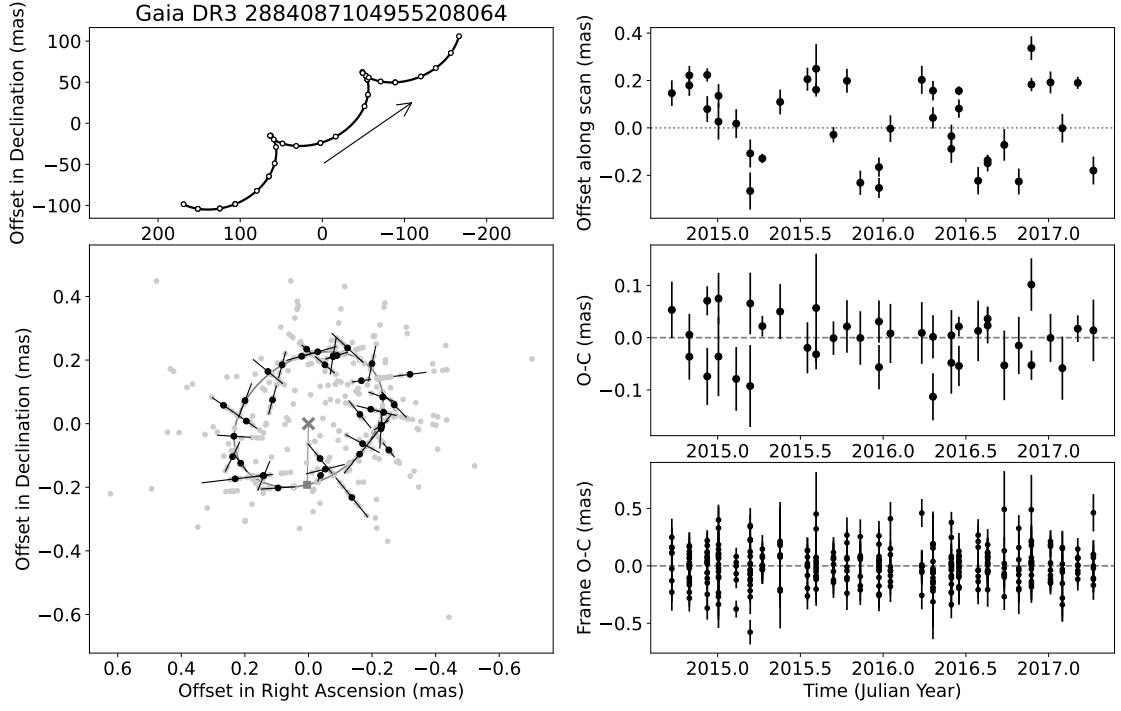


Fig. 15. Same as Fig. 12 but for HD 40503 i.e. Gaia DR3 2884087104955208064 ($G = 8.97$ mag, $P = 826.53 \pm 49.89$ day, $e = 0.07 \pm 0.10$, $\varpi = 25.49 \pm 0.01$ mas).

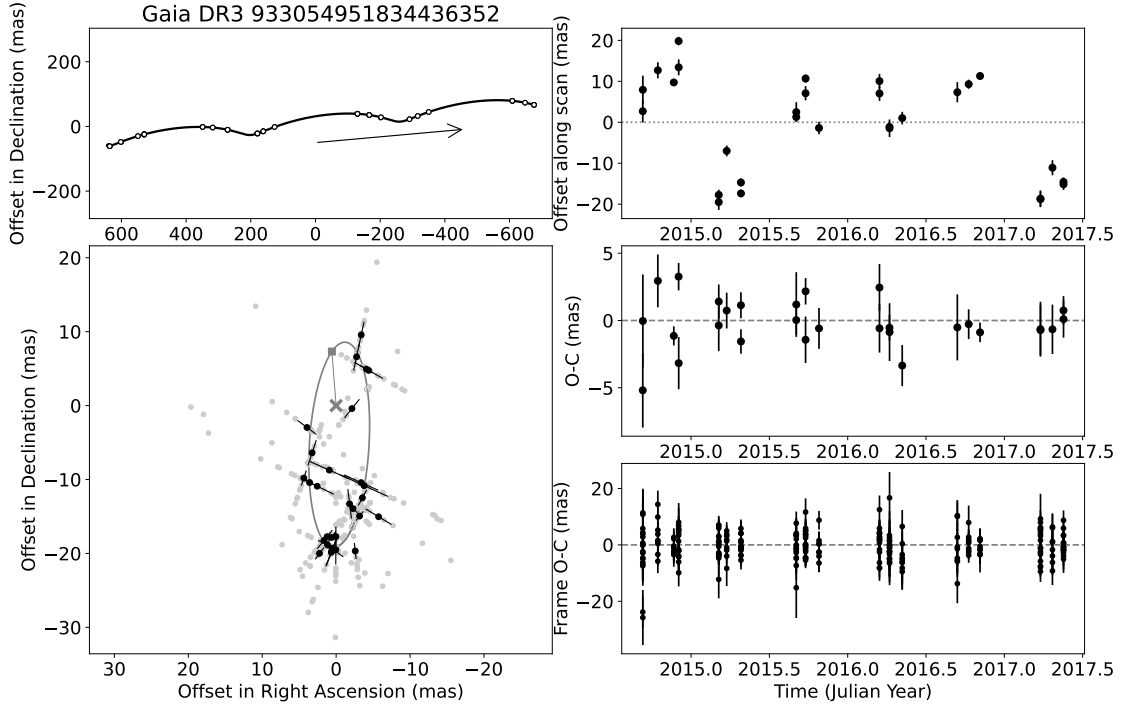


Fig. 16. Same as Fig. 12 but for 2MASS J08053189+4812330 i.e. Gaia DR3 933054951834436352 ($G = 20.01$ mag, $P = 735.91 \pm 22.99$ day, $e = 0.42 \pm 0.23$, $\varpi = 43.77 \pm 0.71$ mas).

cases, inconsistencies between literature RV data and the Gaia solutions were overlooked. Two such examples are those corresponding to Gaia DR3 1748596020745038208 (WASP-2) and Gaia DR3 5656896924435896832 (HATS-26, TOI-574). The two known companions are hot Jupiters with orbital periods of 2.1 d (Collier Cameron et al. 2007; Knutson et al. 2014) and 3.3 d (Espinoza et al. 2016), respectively. The Gaia solutions have $P = 38$ d and $P = 193$ d, respectively. No additional RV

trends or modulations are detected for WASP-2 and HATS-26, indicating that the Gaia detections might be spurious.

Another illustration of the challenges of the validation procedure is the case of GJ 812A (HIP 103393) for which 9 HARPS measurements were taken between August 2011 and August 2012 that are publicly available on DACE (see Table A.2). The periodogram of the RV time series does not show any significant peak at the Gaia period ($P = 23.926 \pm 0.010$ d) but a compatible

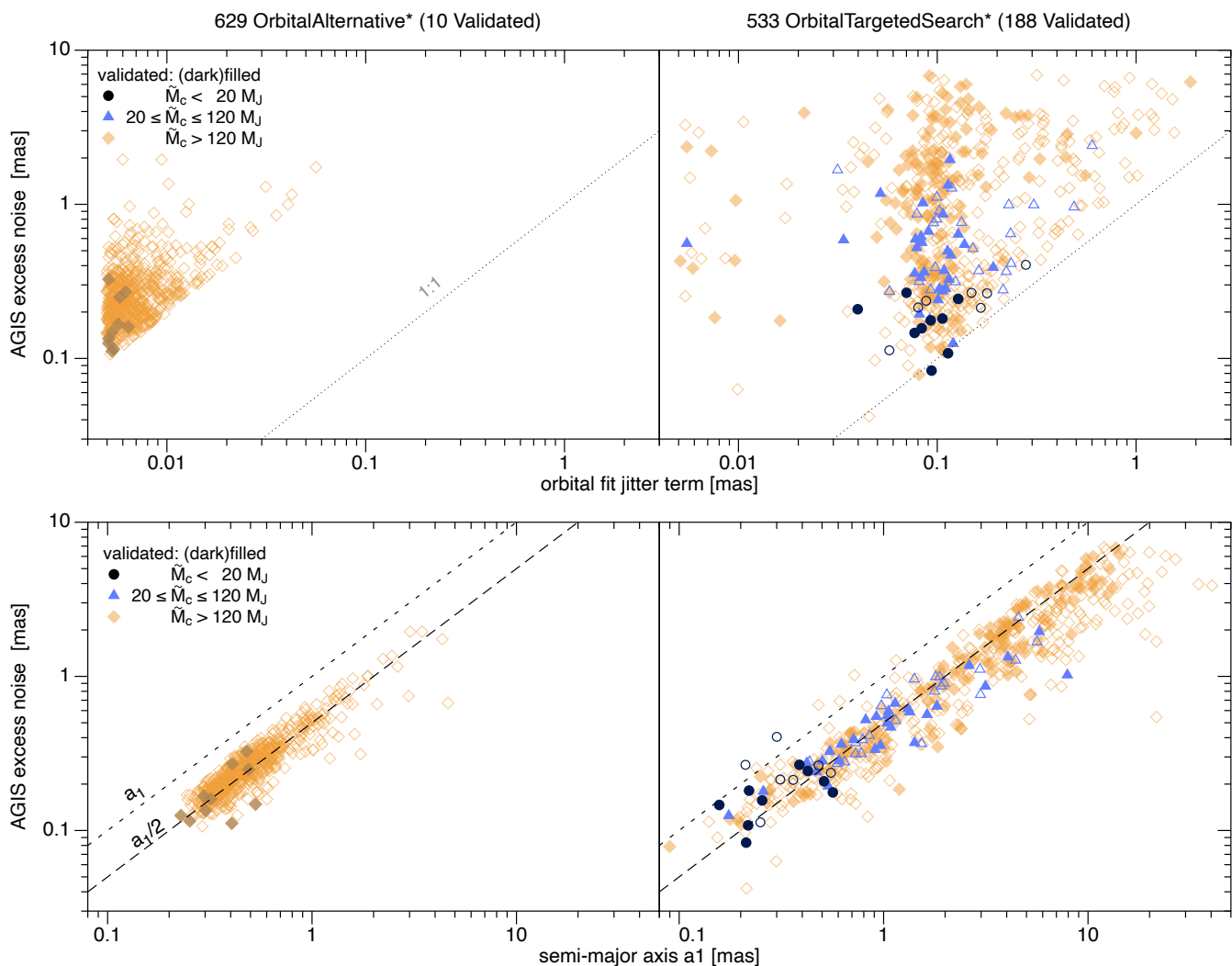


Fig. 17. Comparison with the single-star AGIS excess noise.

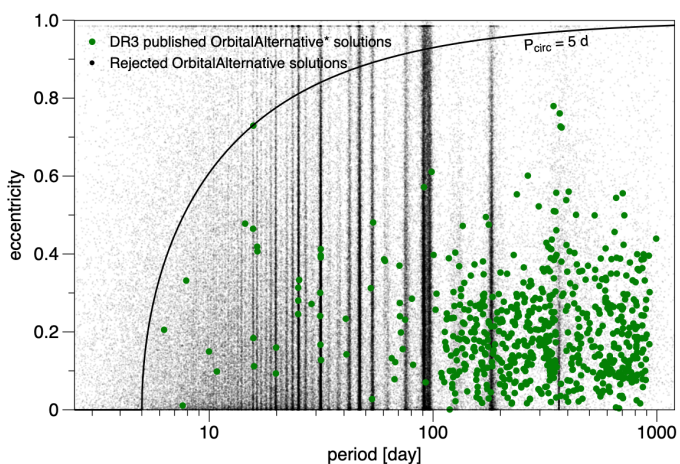


Fig. 18. Period-eccentricity diagram for a random sample of sources (black points) with orbits obtained by the DE-MCMC or GA algorithms from the processing of the stochastic solution sample. The clear structure of period aliases are symptoms of incorrectly derived orbits and are further discussed in Holl et al. (2022). The green filled dots correspond to P and e values from ‘OrbitalAlternative’ solutions. The solid black curve indicates the maximum eccentricity attainable for an orbit unaffected by tides, assuming a cut-off period of 5 days (see e.g. Halbwachs et al. (2005))

RV orbit can be found once the period is fixed to the Gaia period. Furthermore, a close inspection of the HARPS’ CCFs shows that GJ 812A is a double-line spectroscopic binary and rules out the presence of a brown dwarf companion to GJ 812A.

6.3.3. Other literature solutions

Among literature solutions obtained with techniques other than astrometry and RVs, we report in Table A.2 the good agreement between the Gaia period and that obtained by Murphy et al. (2016a) for the companion orbiting Gaia DR3 2075978592919858432 (KIC 7917485, Kepler-1648). The primary is a δ Scuti variable, A-type star, and the companion was identified based on phase modulation of the pulsations of the host.

Among the sample of Kepler transiting planets that have been statistically validated, Kepler-1697b orbits a K-dwarf primary (Gaia DR3 2102991776844251264) with $P = 33.5$ d (Armstrong et al. 2021). The Gaia ‘OrbitalTargetedSearch’ solution has $P = 98.5$ d and $i \approx 65$ deg, which might indicate either a spurious orbit, or the presence of a third body in the system.

A small number of transiting planet candidates from the TESS mission (TESS Objects of Interest, TOIs) are worth mentioning. TOI-288 (Gaia DR3 6608926350294211328), TOI 289 (Gaia DR3 4919562197762515456), TOI-1104

(Gaia DR3 6345896578791113472) and TOI-2008 (Gaia DR3 5096613016130459136) are indicated as single-transit candidates, and the Gaia solutions of type ‘OrbitalTargetedSearchValidated’ have $P = 79$ d, $P = 223$ d, $P = 170$ d, and $P = 52$ d, respectively, and close to edge-on configurations, indicating these are likely to be the companions responsible for the eclipses. In the case of TOI-355 (Gaia DR3 5013703860801457280), the transit candidate has $P = 1.03$ d, while the Gaia solution is validated with $P = 297$ d, indicating the presence of a third body in the system (not necessarily transiting). Similar conclusions could be drawn for TOI-614 (Gaia DR3 570355367386642611), TOI-746 (Gaia DR3 528033714422882547), TOI-946 (Gaia DR3 5549740136101187840), and TOI-1113 (Gaia DR3 6356417496318028928), all found to be hosting short-period transiting planet candidates and for which Gaia solutions of type ‘OrbitalTargetedSearch’ have much longer P values. With no additional external validation, however, they could also correspond to spurious solutions, as in the case of TOI-574 discussed in Sect 6.3.2. For TOI-933 (Gaia DR3 5499342375670742784), the period of the transit candidate is almost exactly twice that fitted in the Gaia astrometry. The latter solution is far from edge-on, which might be a symptom of a spurious solution.

Finally, the case of HD 185501 (Gaia DR3 2047188847334279424) is particularly instructive: the Gaia solution has $P = 450$ d and $a_1 = 0.48$ mas, which at the distance of 32.75 pc (assuming a $1 - M_\odot$ primary) would imply detection of a companion well in the substellar regime. However, speckle imaging data have revealed HD 185501 to be an equal-mass binary with ~ 0.04 arcsec separation and $P = 434$ d (Horch et al. 2020, and references therein). This is to our knowledge the only clear case in the ‘OrbitalTargetedSearch’ sample of a system incorrectly classified as having a low-mass companion with negligible flux ratio, but rather being one with two components having flux ratio very close to the mass ratio (see 6.2.1).

6.3.4. Compatibility with independent Gaia solutions

The overlap with alternative solution published by the Gaia NSS pipeline includes a total of 230 cases: 213 in `nss_two_body_orbit` and 17 in `nss_non_linear_spectro`, as tabulated in Tab. 2. See Appendix B for the related queries. Our sample has no overlap with the `nss_acceleration_astro` and `nss_vim_fl` solution tables.

Generally, a given source can have solutions of different `nss_solution_type` in `nss_two_body_orbit`, except for solutions that were obtained from astrometric data only, i.e. an ‘OrbitalTargetedSearch[Validated]’ solution would supersede an ‘Orbital’ solution. For the ten ‘OrbitalAlternativeValidated’ sources the alternative, and completely independent ‘SB1’ solutions, have compatible periods (to within 10%) and eccentricities with respect to the orbital solutions from our exoplanet pipeline, and thus were used to provide these sources with the ‘Validated’ suffix. They are listed in Appendix A. Similarly, out of 147 ‘OrbitalAlternativeValidated’ sources with alternative Gaia solutions, 142 were found to have matching period to within 10% with solutions of different `nss_solution_type` in `nss_two_body_orbit`.

The identification of discrepant orbital solutions for the same `source_id` in Gaia astrometry, spectroscopy and/or photometry does not necessarily mean that either one is incorrect as their respective sensitivities are largely non-overlapping, especially for the lower mass regime, thus they may correspond to effects induced by different components of the system. No sources were thus filtered out based on this Gaia internal comparison.

Five ‘OrbitalTargetedSearchValidated’ sources have orbital periods differing by more than 10% from those of other Gaia solutions. Gaia DR3 4748772376561143424, Gaia DR3 3309006602007842048, and Gaia DR3 276487905502478720 have ‘AstroSpectroSB1’ and ‘SB1’ (the latter two) long-period solutions, which appear compatible with the fitted values from astrometry. The ‘SB1’ solution for Gaia DR3 3550762648877966336 has $P = 6.8$ d, while the astrometric orbit has $P = 1213$ d. Based on criteria of significance of the semi-major axis and RV semi-amplitude of the astrometric and spectroscopic orbit and period ratios such as the ones listed in Gaia Collaboration et al. (2022), the system is robustly classified as a hierarchical triple. As for Gaia DR3 2370173652144123008, this is discussed further in the following section.

A total of 57 sources have ‘OrbitalTargetedSearch’ solutions as well as another orbital solution of type: ‘SB1’, ‘SB2’, ‘SB2C’, ‘EclipsingSpectro’, or ‘AstroSpectroSB1’. Of these, 48 have period discrepancies in excess of 10%. For 22 of them both periods are > 750 d, so they can be considered compatible on the grounds of the expectedly larger uncertainties as P is similar to, or exceeds the DR3 timespan of the observations. Seven sources with astrometric orbits with $P > 330$ d have additional short-period solutions (1 ‘EclipsingSpectro’: Gaia DR3 5556931152602576000; 3 ‘SB1’: Gaia DR3 3537815929524205568, Gaia DR3 4975005999307397376, Gaia DR3 3775615766054509568; 3 ‘SB2’: Gaia DR3 5963704000561744768, Gaia DR3 3304340751399786752, Gaia DR3 5549740136101187840). These could still be interpreted as triple systems. The remainder of the sources have two solutions with both periods ≤ 120 d. In a few cases (Gaia DR3 529410543928828256, Gaia DR3 2729543564483732608, Gaia DR3 6531037981670835584) the period ratio is approximately 2, but for the majority of the sources the period values do not appear compatible, indicating a fraction of the solutions might be spurious.

For 15 sources with ‘OrbitalTargetedSearch’ orbits (and one ‘OrbitalTargetedSearchValidated’ orbit) the additional Gaia solution is of ‘FirstDegreeTrendSB1’ or ‘SecondDegreeTrendSB1’ type. With one exception, all astrometric orbits have $P > 820$ d, likely indicating that the fitted astrometric orbits have significantly under-estimated the true periods of the companions. This is an expected feature of the orbit fitting process in the limit of periods longer than the timespan of the Gaia observations (e.g., Casertano et al. 2008). For Gaia DR3 5140730507877918592, the $P \approx 53$ d orbit might possibly be spurious.

Overall, based on the above consideration we roughly estimate a degree of contamination from spurious solutions of $\sim 10\%$ in the ‘OrbitalTargetedSearch’ sample.

6.3.5. Solutions of particular interest

Three ‘OrbitalTargetedSearch[Validated]’ solutions imply the discovery of previously-unknown planetary-mass companions if a diluted binary scenario can be discarded. These refer to HIP 66074, HD 40503 and HD 68638A which properties are discussed in Gaia Collaboration et al. (2022).

HIP 66074 has 11 radial velocity measurements taken with the HIRES instrument (Butler et al. 2017) which show a significant dispersion (11 m/s) compared to the measurement uncertainties (1.5 m/s). Fitting the RV data with a constant model and a jitter term ($\sigma_{RV_{jit}}$) results in a $\log(\text{likelihood}) = -37.82$ and $\sigma_{RV_{jit}} = 10.5 \pm 2.5$ m/s. A thorough frequency analysis of the radial velocity time series is not possible due to the limited num-

ber of measurements, but we can nevertheless assess whether the radial velocities are compatible with the Gaia orbit solution: To do so, we fitted a single Keplerian model to the radial velocity with an additional jitter term while keeping the period, the eccentricity, and the argument of periastron fixed at the Gaia-derived values (i.e. $P=297.6$ d; $e=0.46$ and $\omega = 263.11$ deg.). The adjustment converges to $\log(\text{likelihood}) = -18.45$, with $\sigma_v = 0.4 \pm 1.2$ m/s and $T'_0 = 57\,420.044 \pm 0.86$ MJD which is compatible within 1σ with the Gaia-derived value of $T_0 = 57\,443.7 \pm 31.4$ MJD. The comparison between the two RV models based on ΔBIC favours the single Keplerian model with a highly-significant value of $\Delta\text{BIC} = -34$. Assuming the exoplanet scenario is correct, Gaia Collaboration et al. (2022) report a value of $7.3 \pm 1.1 M_{\text{Jup}}$ for the companion.

HD 40503 (HIP 28193) has 4 HARPS and 13 CORALIE radial velocity measurements taken between Dec 2003 and Nov 2021 that are publicly available on DACE (see Table A.2). With a chromospheric activity index of $\log R'_{\text{HK}} = 4.55 \pm 0.02$ derived from the HARPS spectra, the K2 dwarf is considered as active which makes the analysis of the few publicly available RV measurements challenging. The periodogram of the RV time series is also impacted by the sparsity of the data and the different instrumental offsets. It can nevertheless be used to validate the Gaia-orbit. Two dominant peaks at 748 d and 917 d are within 2σ of the Gaia-derived period ($P = 826 \pm 50$ d). In addition, the corresponding Keplerian solutions both lead to a significant improvement of the $\Delta\text{BIC} = -52$ compared to the constant model with an additional RV jitter term. However, due to the limited number of high-resolution spectra and RV measurements, we are not able to rule out the scenario of a blended double-line spectroscopic binary which would require a better phase coverage of the orbital period.

HD 68638A (HIP 40497) has 27 ELODIE radial velocity measurements taken between Nov 1997 and Nov 2003 that are publicly available on DACE (see Table A.2). The periodogram of the RV time series shows a significant peak at 243 days with a FAP lower than 0.01. The corresponding Keplerian solution derived using DACE leads to a significant improvement of the $\Delta\text{BIC} = -85$ compared to the constant model with an additional RV jitter term and a period $P = 240.85 \pm 0.38$ d that is compatible with the Gaia-derived period (241.6 ± 1.0 d). However, Busà et al. (2007) describe the target as a double-line spectroscopic binary - which is confirmed by an inspection of the ELODIE's CCFs available on the "Observatoire de Haute-Provence" archive - ruling out the substellar nature of the companion.

6.3.6. Compatibility with reference data

For 194 sources (of which 188 validated) we have a reference period and eccentricity available, as listed in Appendix A. Here we plot the period and eccentricity compatibility in Fig. 20 and 21, respectively. In the left panels ('OrbitalAlternativeValidated'), the reference data is exclusively from the Gaia 'SB1' solutions.

In the bottom panels of each figure we plot the uncertainly normalised absolute differences (assuming independent solutions and normal distributed uncertainties), so-as to get an idea of the X-sigma offset between the the reference and fitted values. As shown, the vast majority lies within ± 3 sigma, with only a dozen or so beyond it. The most notable 'outliers' are the periods of HD21703 (5086152743542494592, $p_{\text{ref}} = 4.0199$ d) and BD-18113 (2370173652144123008, $p_{\text{ref}} = 10.3$ d) which are different by 0.04 and 7.3 d, respectively. Together with very small uncertainties in both astrometric and literature RV period this causes the large divergence which we accepted in this case.

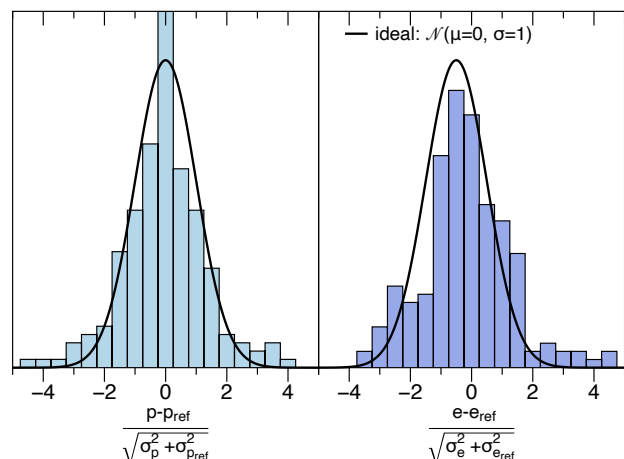


Fig. 19. Distribution of normalised reference value offsets for the 184 solutions in the 'OrbitalTargetedSearch[Validated]' sample.

In Fig. 19 we see that for the 'OrbitalTargetedSearch[Validated]' samples the normalised $p - p_{\text{ref}}$ distributions is reasonably well represented by the expected normal distribution centred around 0 with standard deviation 1, while the normalized $e - e_{\text{ref}}$ distribution has a rather non-Gaussian shape with excesses and deficiencies on both positive and negative side, as also clearly visible in Fig. 21. The median offset -0.22 indicates that overall we tend to fit smaller eccentricities.

7. Conclusions

We present a sample of 1162 orbital solutions of Gaia astrometric data produced by the exoplanet pipeline, spanning the planetary mass regime up to low-mass stellar companions and probing a low astrometric signal-to-noise regime. The host-star distribution is dominated by main-sequence stars along with a small fraction of (sub-)giant stars spanning the apparent magnitude range of $G \sim 3 - 20$. The vast majority of least massive (potentially brown dwarf and planetary mass) companions are confined to $G \lesssim 11$. Semi-major axes range between $a_1 \sim 0.1 - 10$ mas with the majority of periods found between 100 - 2000 d and a noticeable tail down to ~ 8 d. The least massive companions are detected out to ~ 100 pc, with (sub-)stellar mass companions up to (several) kiloparsecs. The sky distribution is rather uniform for the (nearby) least massive companions and more confined to the Galactic plane for the more massive (further out) ones.

The sample orbital solutions is subdivided in the Gaia DR3 `nss_two_body_orbit` archive table into four `nss_solution_type`: 629 'OrbitalAlternative[Validated]' of which 10 validated and 533 'OrbitalTargetedSearch[Validated]' of which 188 validated (Sect. 5).

Due to the rather short available time span of 34 months of data, limited number of observations, and still to be improved error model (in particular calibrations) in the bright-star regime, we had to adopt a complex, inhomogeneous filtering procedure, and a large variety of verification and validation steps (often on source-per-source basis) in order to present a sample with high reliability (i.e. low contamination from spurious solutions and incorrectly classified objects) at the cost of very low completeness and very uneven selection function. We estimate the level of spurious/incorrect solutions in our sample to be of the order of $\sim 5\%$ and $\sim 10\%$ in the 'OrbitalAlternative' and 'OrbitalTargetedSearch' sample, respectively.

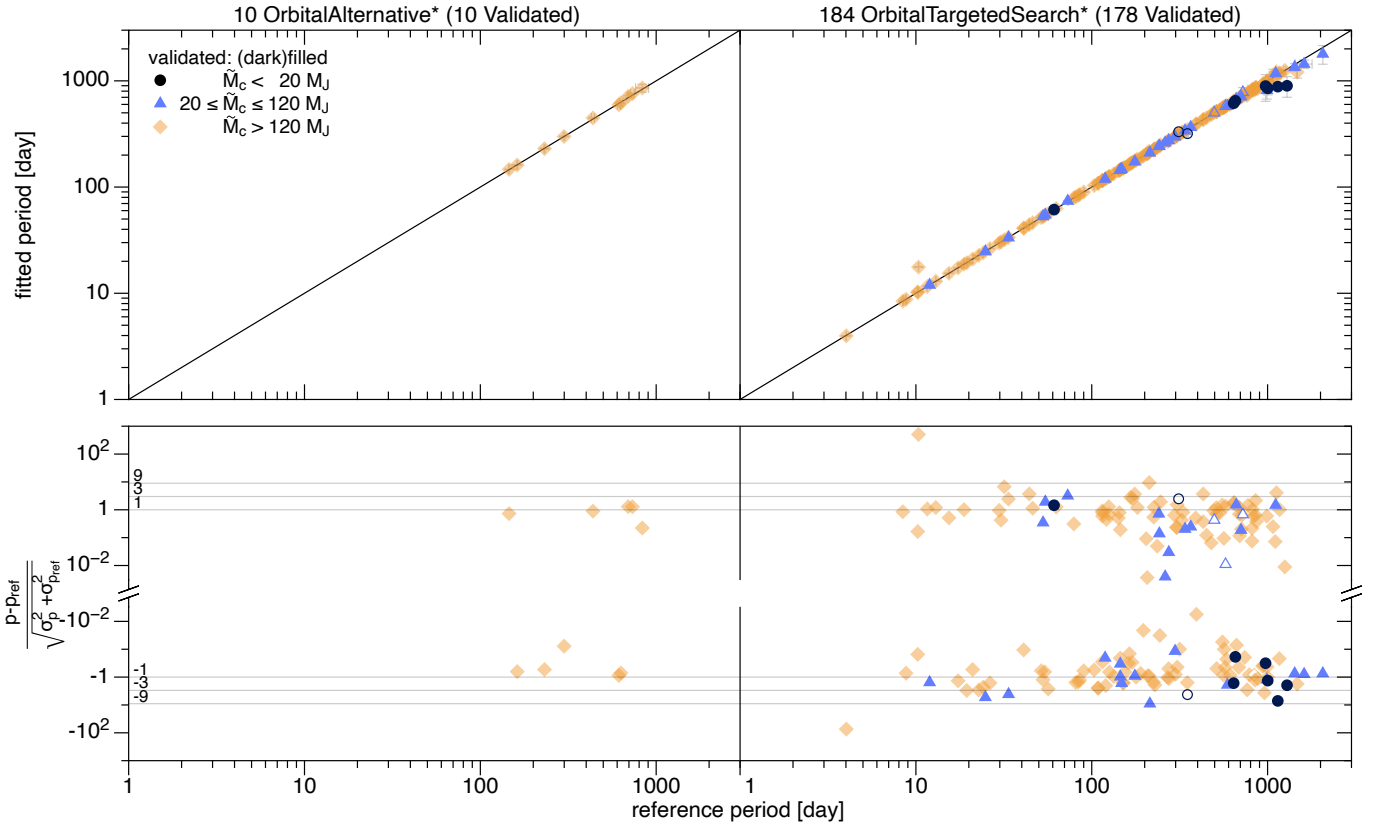


Fig. 20. Period versus reference period of sources with reference data available.

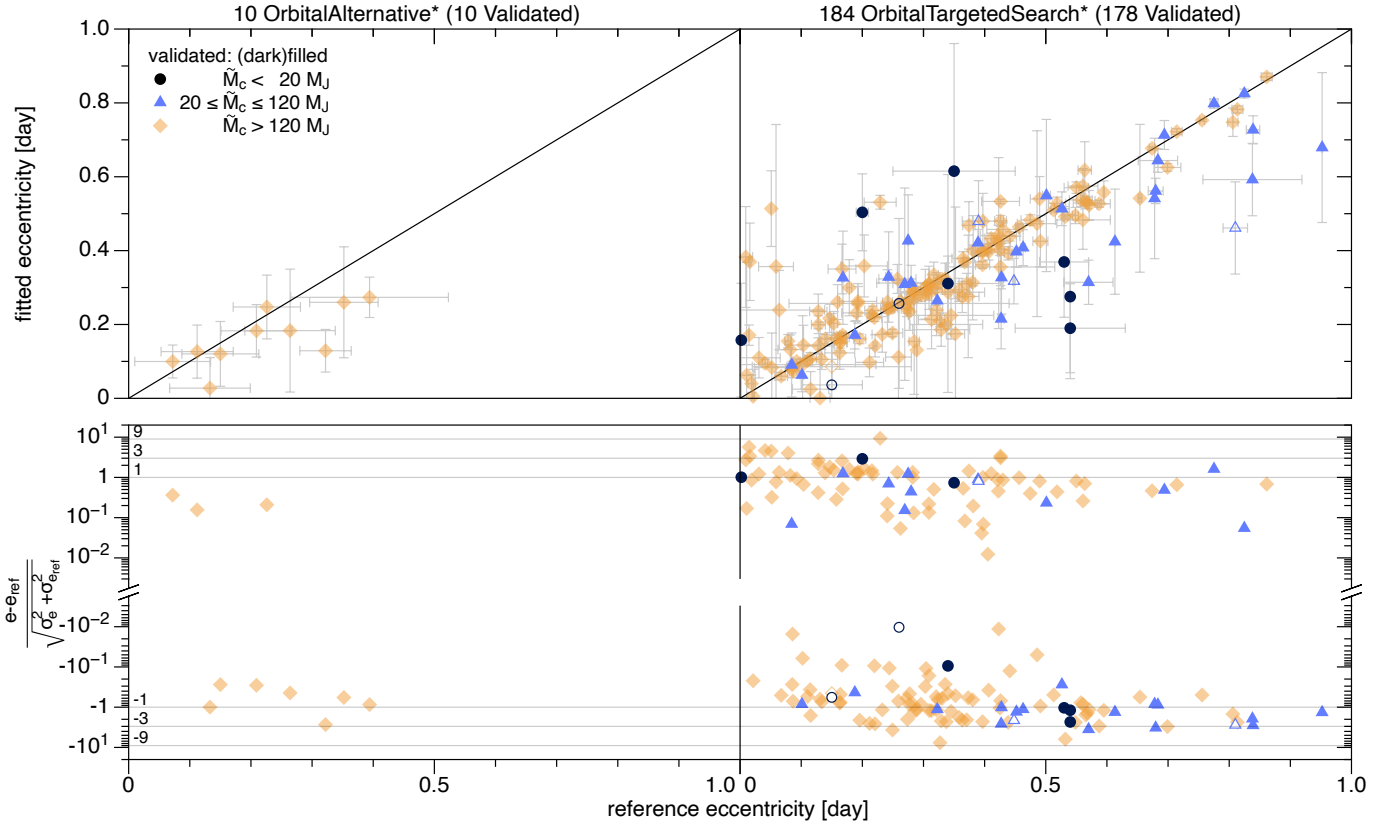


Fig. 21. Eccentricity versus reference eccentricity of sources with reference data available.

Given the above mentioned difficulties, it is therefore no surprise that the Gaia DR3 sample of (known and new) exoplanets and brown dwarfs orbiting bright F-G-K dwarfs with reliable as-

tronomical orbits is small⁸. Over the past two decades, estimates

⁸ See Gaia Collaboration et al. (2022) for a different perspective on the sample of astrometrically detected substellar companions to low-mass M dwarfs.

Table 2. Overview of 213 `source_id`'s with an alternative solution in either `nss_two_body_orbit` or `nss_non_linear_spectro`.

Exoplanet pipeline <code>nss_solution_type</code>	Alternative <code>nss_solution_type</code>	Counts	Alternative table name
'OrbitalAlternative'	'SecondDegreeTrendSB1'	1	<code>nss_non_linear_spectro</code>
'OrbitalAlternativeValidated'	'SB1'	10	<code>nss_two_body_orbit</code>
'OrbitalTargetedSearch'	'SB1'	40	<code>nss_two_body_orbit</code>
'OrbitalTargetedSearch'	'SecondDegreeTrendSB1'	11	<code>nss_non_linear_spectro</code>
'OrbitalTargetedSearch'	'SB2'	9	<code>nss_two_body_orbit</code>
'OrbitalTargetedSearch'	'AstroSpectroSB1'	6	<code>nss_two_body_orbit</code>
'OrbitalTargetedSearch'	'FirstDegreeTrendSB1'	4	<code>nss_non_linear_spectro</code>
'OrbitalTargetedSearch'	'EclipsingSpectro'	1	<code>nss_two_body_orbit</code>
'OrbitalTargetedSearch'	'SB2C'	1	<code>nss_two_body_orbit</code>
'OrbitalTargetedSearchValidated'	'AstroSpectroSB1'	92	<code>nss_two_body_orbit</code>
'OrbitalTargetedSearchValidated'	'SB1'	46	<code>nss_two_body_orbit</code>
'OrbitalTargetedSearchValidated'	'SB2'	8	<code>nss_two_body_orbit</code>
'OrbitalTargetedSearchValidated'	'SecondDegreeTrendSB1'	1	<code>nss_non_linear_spectro</code>

of the Gaia harvest of exoplanets and brown dwarfs (Lattanzi et al. 2000; Sozzetti et al. 2001; Casertano et al. 2008; Sozzetti 2014; Sozzetti et al. 2014; Perryman et al. 2014; Sahlmann et al. 2015b; Holl, B. et al. 2022) have converged on ballpark numbers of (tens of) thousands of new detections. These studies have always provided end-of-mission (nominal or extend) figures, which cannot therefore be directly compared with the DR3-level sensitivity of the Gaia survey. Indeed, Gaia DR3 provides the first-ever full orbital solutions for a number of known exoplanets and brown dwarfs, and allows to identify a few previously unknown planetary-mass companions based on astrometric data alone. This should be regarded by no means a small feat, but rather a fundamental stepping stone for the expected improvements in future data releases.

Acknowledgements. We thank the anonymous referee for helpful feedback and suggestions that improved the quality of this paper. This work has, in part, been carried out within the framework of the National Centre for Competence in Research PlanetS supported by SNSF, A.S., P.G., M.G.L., and R.M. gratefully acknowledge financial support of the Italian Space Agency (ASI) under contracts 2018-24-HH.0 and 2018-24-HH.1-2022 in support of the Italian participation to the Gaia mission. This work presents results from the European Space Agency (ESA) space mission Gaia. Gaia data are being processed by the Gaia Data Processing and Analysis Consortium (DPAC). Funding for the DPAC is provided by national institutions, in particular the institutions participating in the Gaia MultiLateral Agreement (MLA). The Gaia mission website is <https://www.cosmos.esa.int/gaia>. The Gaia archive website is <https://archives.esac.esa.int/gaia>. Acknowledgements are given in Appendix D This publication makes use of the Data & Analysis Center for Exoplanets (DACE), which is a facility based at the University of Geneva (CH) dedicated to extrasolar planets data visualisation, exchange and analysis. DACE is a platform of the Swiss National Centre of Competence in Research (NCCR) PlanetS, federating the Swiss expertise in Exoplanet research. The DACE platform is available at <https://dace.unige.ch>. This research has made use of the NASA Exoplanet Archive, which is operated by the California Institute of Technology, under contract with the National Aeronautics and Space Administration under the Exoplanet Exploration Program. This research has made use of the SIMBAD database, operated at CDS, Strasbourg, France. The authors made use of DATAGRAPH, TOPCAT (Taylor 2005), ASTROPY (a community-developed core Python package for Astronomy (Astropy Collaboration et al. 2013)), SCIPY (Jones et al. 2001), NUMPY (Oliphant 2007), IPYTHON (Pérez & Granger 2007), PANDAS (Reback et al. 2022) and MATPLOTLIB (Hunter 2007).

References

Alcock, C., Allsman, R., Alves, D. R., et al. 2000, *ApJ*, 542, 257
 Armstrong, D. J., Gamper, J., & Damoulas, T. 2021, *MNRAS*, 504, 5327
 Arriagada, P., Butler, R. P., Minniti, D., et al. 2010, *ApJ*, 711, 1229
 Astropy Collaboration, Robitaille, T. P., Tollerud, E. J., et al. 2013, *A&A*, 558, A33
 Babusiaux, C., Fabricius, C., & et al. 2022, *A&A* in prep.
 Barbato et al. 2022, *A&A* in prep.

Binnendijk, L. 1960, Properties of double stars; a survey of parallaxes and orbits.
 Bonfils, X., Delfosse, X., Udry, S., et al. 2013, *A&A*, 549, A109
 Bouchy, F., Hébrard, G., Udry, S., et al. 2009, *A&A*, 505, 853
 Busà, I., Aznar Cuadrado, R., Terranegra, L., Andretta, V., & Gomez, M. T. 2007, *A&A*, 466, 1089
 Butler, R. P., Tinney, C. G., Marcy, G. W., et al. 2001, *ApJ*, 555, 410
 Butler, R. P., Vogt, S. S., Laughlin, G., et al. 2017, *AJ*, 153, 208
 Butler, R. P., Wright, J. T., Marcy, G. W., et al. 2006, *ApJ*, 646, 505
 Casertano, S., Lattanzi, M. G., Sozzetti, A., et al. 2008, *A&A*, 482, 699
 Collier Cameron, A., Bouchy, F., Hébrard, G., et al. 2007, *MNRAS*, 375, 951
 da Silva, R., Udry, S., Bouchy, F., et al. 2007, *A&A*, 473, 323
 Dalal, S., Kiefer, F., Hébrard, G., et al. 2021, *A&A*, 651, A11
 Delisle, J. B. & Ségransan, D. 2022, Analytical determination of orbital elements using Fourier analysis. II. Gaia astrometry and its combination with radial velocities
 Doyle, L. R., Carter, J. A., Fabrycky, D. C., et al. 2011, *Science*, 333, 1602
 Drimmel, R., Sozzetti, A., Schröder, K.-P., et al. 2021, *MNRAS*, 502, 328
 Eastman, J., Gaudi, B. S., & Agol, E. 2013, *PASP*, 125, 83
 Espinoza, N., Bayliss, D., Hartman, J. D., et al. 2016, *AJ*, 152, 108
 Evans et al. 2022, *A&A* in prep.
 Eyer et al. 2022, *A&A* in prep.
 F. van Leeuwen, ed. 2007, *Astrophysics and Space Science Library*, Vol. 350, Hipparcos, the New Reduction of the Raw Data
 Feng, F., Crane, J. D., Xuesong Wang, S., et al. 2019, *ApJS*, 242, 25
 Ford, E. B. 2006, *ApJ*, 642, 505
 Gaia Collaboration, Arenou, F., Babusiaux, C., et al. 2022, arXiv e-prints, arXiv:2206.05595
 Gaia Collaboration, Prusti, T., de Bruijne, J. H. J., et al. 2016, *A&A*, 595, A1
 Giammichele, N., Bergeron, P., & Dufour, P. 2012, *ApJS*, 199, 29
 Górski, K. M., Banday, A. J., Hivon, E., & Wandelt, B. D. 2002, in *Astronomical Society of the Pacific Conference Series*, Vol. 281, *Astronomical Data Analysis Software and Systems XI*, ed. D. A. Bohlender, D. Durand, & T. H. Handley, 107
 Halbwachs, J. L., Arenou, F., Mayor, M., Udry, S., & Queloz, D. 2000, *A&A*, 355, 581
 Halbwachs, J. L., Mayor, M., & Udry, S. 2005, *A&A*, 431, 1129
 Halbwachs, J.-L. et al. 2022, *A&A*
 Halbwachs et al. 2022, *A&A* in prep.
 Hébrard, G., Arnold, L., Forveille, T., et al. 2016, *A&A*, 588, A145
 Hełminiak, K. G., Brahm, R., Ratajczak, M., et al. 2014, *A&A*, 567, A64
 Holl, B., Fabricius, C., & Portell, J. e. 2022, *A&A*, in prep.
 Holl, B., Perryman, M., Lindegren, L., Ségransan, D., & Raimbault, M. 2022, *A&A*, 661, A151
 Holland, J. H. 1975, *Adaptation in Natural and Artificial Systems* (Ann Arbor, MI: University of Michigan Press), second edition, 1992
 Horch, E. P., van Belle, G. T., Davidson, James W. J., et al. 2020, *AJ*, 159, 233
 Hunter, J. D. 2007, *Computing in Science and Engineering*, 9, 90
 Jones, E., Oliphant, T., Peterson, P., et al. 2001, *SciPy: Open source scientific tools for Python*
 Jong, K. D. 1988, *MACHINE LEARNING*, 3, 123
 Kane, S. R., Henry, G. W., Dragomir, D., et al. 2011, *ApJ*, 735, L41
 Kiefer, F., Hébrard, G., Sahlmann, J., et al. 2019, *A&A*, 631, A125
 Kipping, D. M. 2013, *MNRAS*, 434, L51
 Knutson, H. A., Fulton, B. J., Montet, B. T., et al. 2014, *ApJ*, 785, 126
 Kovács, G., Zucker, S., & Mazeh, T. 2002, *A&A*, 391, 369
 Latham, D. W., Stefanik, R. P., Torres, G., et al. 2002, *AJ*, 124, 1144
 Lattanzi, M. G., Spagna, A., Sozzetti, A., & Casertano, S. 2000, *MNRAS*, 317, 211

- Lindgren, L., Klioner, S. A., Hernández, J., et al. 2021, *A&A*, 649, A2
- Lomb, N. R. 1976, *Ap&SS*, 39, 447
- Martin, D. V., Triaud, A. H. M. J., Udry, S., et al. 2019, *A&A*, 624, A68
- Mayor, M., Pepe, F., Queloz, D., et al. 2003, *The Messenger*, 114, 20
- Mendez, R. A., Claveria, R. M., Orchard, M. E., & Silva, J. F. 2017, *AJ*, 154, 187
- Ment, K., Fischer, D. A., Bakos, G., Howard, A. W., & Isaacson, H. 2018, *AJ*, 156, 213
- Minniti, D., Butler, R. P., López-Morales, M., et al. 2009, *ApJ*, 693, 1424
- Moutou, C., Mayor, M., Lo Curto, G., et al. 2009, *A&A*, 496, 513
- Murphy, S. J., Bedding, T. R., & Shibahashi, H. 2016a, *ApJ*, 827, L17
- Murphy, S. J., Bedding, T. R., & Shibahashi, H. 2016b, *ApJ*, 827, L17
- Oliphant, T. E. 2007, *Computing in Science Engineering*, 9, 10
- Pérez, F. & Granger, B. E. 2007, *Computing in Science and Engineering*, 9, 21
- Perryman, M., Hartman, J., Bakos, G. A., & Lindgren, L. 2014, *ApJ*, 797, 14
- Pourbaix et al. 2022, Gaia DR3 documentation Chapter 7: Non-single stars, Online documentation
- Psaridi, A., Bouchy, F., Lendl, M., et al. 2022, *A&A*, 664, A94
- Ranalli, P., Hobbs, D., & Lindgren, L. 2018, *A&A*, 614, A30
- Reback, J., jbrockmendel, McKinney, W., et al. 2022, *pandas-dev/pandas: Pandas 1.4.2*
- Rosenthal, L. J., Fulton, B. J., Hirsch, L. A., et al. 2021, *ApJS*, 255, 8
- Sahlmann, J. 2019, *Johannes-Sahlmann/pystrometry*
- Sahlmann, J., Burgasser, A. J., Bardalez Gagliuffi, D. C., et al. 2020, *MNRAS*, 495, 1136
- Sahlmann, J., Lazorenko, P. F., Ségransan, D., et al. 2015a, *A&A*, 577, A15
- Sahlmann, J., Lazorenko, P. F., Ségransan, D., et al. 2013, *A&A*, 556, A133
- Sahlmann, J., Ségransan, D., Queloz, D., et al. 2011a, *A&A*, 525, A95+
- Sahlmann, J., Ségransan, D., Queloz, D., et al. 2011b, *A&A*, 525, A95
- Sahlmann, J., Triaud, A. H. M. J., & Martin, D. V. 2015b, *MNRAS*, 447, 287
- Scargle, J. D. 1982, *ApJ*, 263, 835
- Schwarz, G. E. 1978, *Annals of Statistics*, 6, 461
- Ségransan, D., Mayor, M., Udry, S., et al. 2011, *A&A*, 535, A54
- Sion, E. M., Holberg, J. B., Oswald, T. D., et al. 2014, *AJ*, 147, 129
- Skuljan, J., Ramm, D. J., & Hearnshaw, J. B. 2004, *MNRAS*, 352, 975
- Smart, R. L., Marocco, F., Sarro, L. M., et al. 2019, *MNRAS*, 485, 4423
- Sozzetti, A. 2014, *Mem. Soc. Astron. Italiana*, 85, 643
- Sozzetti, A., Casertano, S., Lattanzi, M. G., & Spagna, A. 2001, *A&A*, 373, L21
- Sozzetti, A., Giacobbe, P., Lattanzi, M. G., et al. 2014, *MNRAS*, 437, 497
- Sozzetti, A., Udry, S., Zucker, S., et al. 2006, *A&A*, 449, 417
- Taylor, M. B. 2005, in *Astronomical Society of the Pacific Conference Series*, Vol. 347, *Astronomical Data Analysis Software and Systems XIV*, ed. P. Shopbell, M. Britton, & R. Ebert, 29
- Ter Braak, C. J. F. 2006, *Statistics and Computing*, 16, 239
- Tinney, C. G., Butler, R. P., Marcy, G. W., et al. 2001, *ApJ*, 551, 507
- Triaud, A. H. M. J., Martin, D. V., Ségransan, D., et al. 2017, *A&A*, 608, A129
- Triaud, A. H. M. J., Standing, M. R., Heidari, N., et al. 2022a, *MNRAS*[arXiv:2112.06584]
- Triaud, A. H. M. J., Standing, M. R., Heidari, N., et al. 2022b, *MNRAS*, 511, 3561
- Udry, S., Mayor, M., Naef, D., et al. 2002, *A&A*, 390, 267
- Udry, S., Mayor, M., Naef, D., et al. 2000, *A&A*, 356, 590
- Vallenari, A. 2022, *A&A* in prep.
- Wenger, M., Ochsenbein, F., Egret, D., et al. 2000, *A&AS*, 143, 9
- Wilson, E. B. & Hilferty, M. M. 1931, *Proceedings of the National Academy of Science*, 17, 684
- Wilson, P. A., Hébrard, G., Santos, N. C., et al. 2016, *A&A*, 588, A144
- Wright, J. T. & Howard, A. W. 2009, *ApJS*, 182, 205
- Zechmeister, M. & Kürster, M. 2009, *A&A*, 496, 577

Appendix A: Reference solution parameters

Table A.1, A.2, A.3, and A.4 contain an overview of all sources we published into Gaia DR3 table `nss_two_body_orbit` for which we identified reference data. The precision in the numbers in the printed table is occasionally truncated, but has been preserved in the online table version. Asymmetric uncertainties available for some of the literature sources have been set to the largest absolute uncertainty. The last column contains an index relating to our pseudo-companion mass estimate \tilde{M}_c assuming a solar-mass host, with $0 = \{ \tilde{M}_c < 20 M_J \}$, $1 = \{ 20 M_J \leq \tilde{M}_c \leq 120 M_J \}$, and $2 = \{ \tilde{M}_c > 120 M_J \}$.

Note that for several sources the non-Gaia RV reference parameters are not provided: this corresponds to sources mentioned in Sect. 6.3.2 for which the literature radial velocity by itself did not provide a constrained orbital solution, but the data is consistent with astrometric orbital period. Three validated solutions marked with "†" were validated based on internal Gaia reference data, which was eventually not published in Gaia DR3, therefore no reference values are provided. All sources with available period and eccentricity were used in the analyses of Sect. 6.3.6.

References to data that is publicly available on the Data and Analysis Center for Exoplanets (DACE) platform are marked with "*" and can be directly queried online as indicated in the note of Table A.2.

The HARPS and CORALIE radial velocity light curve for HD40503 has been published as part of this paper in the online material.

Table A.1. Reference solution parameters for ‘OrbitalAlternative[Validated]’ solutions. See Appendix A for details.

nss_solution_type	Gaia DR3 source_id	Name	Ref.	Ref. P [d]	Our P [d]	Ref. e	Our e	\bar{M}_c
‘OrbitalAlternativeValidated’	4517375515957545216		1a	231.7 ± 1.5	229.9 ± 2.9	0.35 ± 0.06	0.26 ± 0.15	2
‘OrbitalAlternativeValidated’	2009052252148821632		1a	630.6 ± 9.4	620.9 ± 9.8	0.23 ± 0.06	0.25 ± 0.09	2
‘OrbitalAlternativeValidated’	6350499649858805120		1a	162.1 ± 1.0	161.3 ± 0.7	0.13 ± 0.07	0.03 ± 0.08	2
‘OrbitalAlternativeValidated’	426186585428243840		1a	693.3 ± 9.2	714.0 ± 13.0	0.32 ± 0.04	0.13 ± 0.06	2
‘OrbitalAlternativeValidated’	5545870301853637504		1a	437.1 ± 8.9	447.3 ± 7.1	0.15 ± 0.06	0.12 ± 0.09	2
‘OrbitalAlternativeValidated’	5431358403498310656		1a	733.3 ± 17.6	757.8 ± 7.4	0.11 ± 0.06	0.13 ± 0.07	2
‘OrbitalAlternativeValidated’	5941647007018169728		1a	834.2 ± 70.8	856.7 ± 72.5	0.26 ± 0.07	0.18 ± 0.17	2
‘OrbitalAlternativeValidated’	2274022837765746304		1a	145.7 ± 1.2	146.6 ± 0.3	0.39 ± 0.13	0.27 ± 0.05	2
‘OrbitalAlternativeValidated’	2055801936074059264		1a	613.6 ± 11.7	596.7 ± 15.4	0.07 ± 0.06	0.10 ± 0.04	2
‘OrbitalAlternativeValidated’	513567110946268544		1a	299.6 ± 3.3	299.3 ± 2.0	0.21 ± 0.06	0.18 ± 0.07	2

References. (1a) Gaia DR3 table nss_two_body_orbit with nss_solution_type = SB1;

Table A.2. Non-Gaia reference solution parameters for ‘OrbitalTargetedSearch[Validated]’ solutions. See Appendix A for details.

nss_solution_type	Gaia DR3 source_id	Name	Ref.	Ref. P [d]	Our P [d]	Ref. e	Our e	M_c
‘OrbitalTargetedSearchValidated’	1318110830190386048	HD148284	4	$339.3 \pm 2e-2$	339.6 ± 1.2	$0.39 \pm 9e-4$	0.42 ± 0.04	1
‘OrbitalTargetedSearchValidated’	409909484005053440	HD8054	5	847.7 ± 3.8	835.4 ± 8.8	0.81 ± 0.01	0.75 ± 0.04	2
‘OrbitalTargetedSearchValidated’	4062446910648807168	HD164604	6	641.5 ± 10.1	615.5 ± 12.0	0.35 ± 0.10	0.62 ± 0.35	0
‘OrbitalTargetedSearchValidated’	6374231714992810752	EBLM J2011-71	7	663.0 ± 0.3	671.5 ± 5.6	$0.10 \pm 3e-3$	0.06 ± 0.05	1
‘OrbitalTargetedSearchValidated’	2370173652144123008	BD-18113	31*	$10.3 \pm 1e-6$	$17.6 \pm 1e-2$	$0.05 \pm 6e-5$	0.51 ± 0.10	2
‘OrbitalTargetedSearchValidated’	873616860770228352	BD+291539	8	$175.9 \pm 1e-2$	173.2 ± 3.0	$0.27 \pm 1e-3$	0.43 ± 0.12	1
‘OrbitalTargetedSearchValidated’	1142214430312151424	HD48679	8	1111.6 ± 0.3	1177.8 ± 45.0	$0.82 \pm 5e-4$	0.83 ± 0.01	1
‘OrbitalTargetedSearchValidated’	3550762648877966336	HD94340	3	1122.7 ± 0.4	1213.8 ± 22.0	$0.30 \pm 3e-3$	0.30 ± 0.01	2
‘OrbitalTargetedSearchValidated’	3626268998574790656	HD112758	9	$103.3 \pm 3e-2$	$103.2 \pm 3e-2$	0.14 ± 0.01	0.16 ± 0.01	2
‘OrbitalTargetedSearchValidated’	6264881882000588672	HD137812	3	$73.0 \pm 3e-4$	73.9 ± 0.3	$0.61 \pm 6e-4$	0.42 ± 0.14	1
‘OrbitalTargetedSearchValidated’	2603090003484152064	GI876	10	$61.0 \pm 8e-4$	61.4 ± 0.2	$2e-3 \pm 2e-3$	0.16 ± 0.15	0
‘OrbitalTargetedSearchValidated’	637329067477530368	HD81040	11	1001.7 ± 7.0	850.8 ± 113	0.53 ± 0.04	0.37 ± 0.15	0
‘OrbitalTargetedSearchValidated’	1035000055055287680	HD68638A	33*	240.9 ± 0.4	241.6 ± 1.0	0.57 ± 0.04	0.31 ± 0.06	1
‘OrbitalTargetedSearchValidated’	1594127865540229888	HD132406	12	974.0 ± 39.0	893.2 ± 251	0.34 ± 0.09	0.31 ± 0.30	0
‘OrbitalTargetedSearchValidated’	6421118739093252224	HD175167	13	1290.0 ± 22.0	898.7 ± 198	0.54 ± 0.09	0.19 ± 0.12	0
‘OrbitalTargetedSearchValidated’	5957920668132624256	HD162020	14	$8.4 \pm 6e-5$	$8.4 \pm 1e-3$	$0.28 \pm 2e-3$	0.23 ± 0.05	2
‘OrbitalTargetedSearchValidated’	3921176983720146560	HD106888	8	365.6 ± 0.1	366.3 ± 2.8	$0.46 \pm 4e-3$	0.41 ± 0.05	1
‘OrbitalTargetedSearchValidated’	4385502286022654464	HD151465	15	$54.4 \pm 2e-3$	54.8 ± 0.2	0.24 ± 0.01	0.33 ± 0.12	1
‘OrbitalTargetedSearchValidated’	5808612830236138368	HD147584	29	$13.0 \pm 1e-5$	$13.0 \pm 1e-3$	$0.01 \pm 4e-4$	0.17 ± 0.03	2
‘OrbitalTargetedSearchValidated’	5086152743542494592	HD21703	30	$4.0 \pm 1e-4$	$4.0 \pm 6e-4$	0.34 ± 0.06	0.29 ± 0.10	2
‘OrbitalTargetedSearchValidated’	685029558383335168	HD77065	16	$119.1 \pm 3e-3$	119.1 ± 0.2	$0.69 \pm 4e-4$	0.71 ± 0.04	1
‘OrbitalTargetedSearchValidated’	3751763647996317056	HD89707	9	$297.7 \pm 6e-3$	297.5 ± 2.0	$0.95 \pm 1e-3$	0.68 ± 0.20	1
‘OrbitalTargetedSearchValidated’	933054951834436352	J0805+4812	17	740.4 ± 1.6	735.9 ± 23.0	0.42 ± 0.02	0.42 ± 0.23	2
‘OrbitalTargetedSearchValidated’	824461960796102528	HD82460	8	590.9 ± 0.2	579.3 ± 6.1	0.84 ± 0.01	0.73 ± 0.04	1
‘OrbitalTargetedSearchValidated’	2367734656180397952	BD-170063	18	655.6 ± 0.6	648.9 ± 36.0	0.54 ± 0.01	0.28 ± 0.22	0
‘OrbitalTargetedSearchValidated’	4994200964065634432	HD3277	19	$46.2 \pm 2e-4$	$46.2 \pm 9e-3$	$0.29 \pm 1e-3$	0.27 ± 0.01	2
‘OrbitalTargetedSearchValidated’	5514929155583865216	J0823-4912	20	246.4 ± 1.4	250.0 ± 1.2	0.35 ± 0.07	0.22 ± 0.06	2
‘OrbitalTargetedSearchValidated’	4753355209745022208	HD17155	3	1426.1 ± 0.7	1346.1 ± 107	$0.78 \pm 6e-3$	0.80 ± 0.01	1
‘OrbitalTargetedSearchValidated’	3309006602007842048	HD30246	16	990.7 ± 5.6	814.7 ± 141	0.84 ± 0.08	0.59 ± 0.10	1
‘OrbitalTargetedSearchValidated’	6608926350294211328	TOI-288	32*	79.1 ± 0.1	79.3 ± 0.5	$0.65 \pm 3e-3$	0.54 ± 0.20	2
‘OrbitalTargetedSearchValidated’	4942195301023352320	HIP9095	3*	960.0 ± 1.4	919.6 ± 10.9	$0.33 \pm 1e-3$	0.21 ± 0.02	2
‘OrbitalTargetedSearchValidated’	5902262122552686848	HD134237	3	774.3 ± 3.4	780.4 ± 2.4	0.43 ± 0.03	0.53 ± 0.01	2
‘OrbitalTargetedSearchValidated’	2161507648230817792	HD166356	15	261.5 ± 0.1	261.5 ± 0.9	$0.45 \pm 4e-3$	0.40 ± 0.04	1
‘OrbitalTargetedSearchValidated’	6647630950597964544	HD164427A	21	$108.6 \pm 4e-2$	$108.4 \pm 4e-2$	0.55 ± 0.02	0.57 ± 0.02	2
‘OrbitalTargetedSearchValidated’	5563001178343925376	HD52756	19	$52.9 \pm 1e-4$	52.9 ± 0.1	$0.68 \pm 3e-4$	0.54 ± 0.16	1
‘OrbitalTargetedSearchValidated’	5294069567720883968	HD63581	3	1472.6 ± 0.2	1210.5 ± 150	$0.59 \pm 1e-3$	0.56 ± 0.03	2
‘OrbitalTargetedSearchValidated’	855523714036230016	HD92320	16	$145.4 \pm 1e-2$	145.1 ± 0.3	$0.32 \pm 1e-3$	0.26 ± 0.05	1
‘OrbitalTargetedSearchValidated’	4724313637321332864	HD17289	19	562.1 ± 0.4	561.7 ± 0.3	$0.53 \pm 4e-3$	$0.49 \pm 5e-3$	2
‘OrbitalTargetedSearchValidated’	1224551770875466496	HD140913	9	$147.9 \pm 3e-2$	147.6 ± 0.2	0.53 ± 0.01	0.51 ± 0.05	1
‘OrbitalTargetedSearchValidated’	5855730584310531200	HD111232	22	1143.0 ± 14.0	882.1 ± 34.0	0.20 ± 0.01	0.50 ± 0.10	0
‘OrbitalTargetedSearchValidated’	6334716469679728000	HD134251	3	$54.0 \pm 1e-4$	53.9 ± 0.1	$0.29 \pm 3e-4$	0.13 ± 0.14	2
‘OrbitalTargetedSearchValidated’	1236764218322666880	HD130396	8	2060.6 ± 7.3	1792.6 ± 359	$0.43 \pm 4e-3$	0.33 ± 0.10	1
‘OrbitalTargetedSearchValidated’	3937211745905473024	HD114762	23	$83.9 \pm 3e-3$	83.7 ± 0.1	$0.34 \pm 5e-3$	0.32 ± 0.04	2
‘OrbitalTargetedSearchValidated’	1181993180456516864	HD132032	16	274.3 ± 0.2	274.4 ± 2.5	$0.08 \pm 2e-3$	0.09 ± 0.09	1
‘OrbitalTargetedSearchValidated’	2133476355197071616	Kepler-16 AB	24	$41.1 \pm 8e-5$	$41.1 \pm 2e-2$	$0.16 \pm 6e-4$	0.26 ± 0.05	2
‘OrbitalTargetedSearchValidated’	1712614124767394816	HIP66074	25	297.6 ± 2.7	297.6 ± 2.7	0.46 ± 0.17	0.46 ± 0.17	0
‘OrbitalTargetedSearchValidated’	2884087104955208064	HD40503	2*	826.5 ± 49.9	826.5 ± 49.9	0.07 ± 0.10	0.07 ± 0.10	0
‘OrbitalTargetedSearchValidated’	276487905502478720	HD26596	*	900.4 ± 7.6	900.4 ± 7.6	0.45 ± 0.01	0.45 ± 0.01	2
‘OrbitalTargetedSearchValidated’	725469767850488064	HD89010	*	523.8 ± 6.2	523.8 ± 6.2	0.59 ± 0.08	0.59 ± 0.08	2
‘OrbitalTargetedSearchValidated’	6913810483612308480	GJ812A	*	$23.9 \pm 1e-2$	$23.9 \pm 1e-2$	0.39 ± 0.02	0.39 ± 0.02	1
‘OrbitalTargetedSearchValidated’	6399966162596931712	GJ9732	*	381.2 ± 0.1	381.2 ± 0.1	0.40 ± 0.01	0.40 ± 0.01	2
‘OrbitalTargetedSearchValidated’	4296383402592198016	HD183162	*	923.5 ± 11.0	923.5 ± 11.0	0.12 ± 0.02	0.12 ± 0.02	2
‘OrbitalTargetedSearchValidated’	5999024986946599808	ISWASPJ152523. 04-463833.9 / CD-46 10046	*	242.5 ± 0.4	242.7 ± 1.6	0.43 ± 0.01	0.22 ± 0.08	1
‘OrbitalTargetedSearch’	2075978592919858432	KIC 7917485	26	840.0 ± 22.0	810.5 ± 28.0	0.15 ± 0.13	0.09 ± 0.06	2
‘OrbitalTargetedSearch’	4745373133284418816	HR 810	27	312.0 ± 5.0	331.7 ± 6.2	0.15 ± 0.05	0.04 ± 0.19	0
‘OrbitalTargetedSearch’	2778298280881817984	HD5433	15	576.6 ± 1.6	576.7 ± 11.0	0.81 ± 0.02	0.46 ± 0.12	1
‘OrbitalTargetedSearch’	3750881083756656128	HD91669	16	497.5 ± 0.6	500.5 ± 6.9	$0.45 \pm 2e-3$	0.32 ± 0.06	1
‘OrbitalTargetedSearch’	4976894960284258048	HD142	28	350.3 ± 3.6	318.6 ± 6.5	0.26 ± 0.18	0.26 ± 0.23	0
‘OrbitalTargetedSearch’	2651390587219807744	BD-004475	15	723.2 ± 0.7	780.0 ± 84.0	0.39 ± 0.01	0.48 ± 0.11	1

References. (2) RV data published with this work; (3) Barbato et al. (2022); (4) Ment et al. (2018); (5) Latham et al. (2002); (6) Feng et al. (2019); (7) Martin et al. (2019); (8) Kiefer et al. (2019); (9) Halbwachs et al. (2000); (10) Rosenthal et al. (2021); (11) Sozzetti et al. (2006); (12) da Silva et al. (2007); (13) Arriagada et al. (2010); (14) Udry et al. (2002); (15) Dalal et al. (2021); (16) Wilson et al. (2016); (17) Sahlmann et al. (2020); (18) Moutou et al. (2009); (19) Sahlmann et al. (2011b); (20) Sahlmann et al. (2013); (21) Tinney et al. (2001); (22) Minniti et al. (2009); (23) Kane et al. (2011); (24) Doyle et al. (2011); (25) Butler et al. (2017); (26) Murphy et al. (2016b); (27) Butler et al. (2001); (28) Butler et al. (2006); (29) Skuljan et al. (2004); (30) Helminiak et al. (2014); (31) Triaud et al. (2017); (32) Psaridi et al. (2022); (33) Reference RV orbital parameters derived from analyses on DACE platform using public data.

Notes. * : data available on: <https://dace.unige.ch/radialVelocities/?pattern=Name> with ‘Name’ the value from that column.

Table A.3. Gaia reference solution parameters for ‘OrbitalTargetedSearchValidated’ solutions, 1 of 2. See Appendix A for details.

nss_solution_type	Gaia DR3 source_id	Name	Ref.	Ref. P [d]	Our P [d]	Ref. e	Our e	M_c
‘OrbitalTargetedSearchValidated’	4919562197762515456	TOI-289	1a	224.7 ± 0.9	222.8 ± 0.9	0.20 ± 0.04	0.36 ± 0.08	2
‘OrbitalTargetedSearchValidated’	3280086388180617600	HD27642	1a	706.1 ± 16.6	709.7 ± 9.1	0.28 ± 0.06	0.31 ± 0.05	1
‘OrbitalTargetedSearchValidated’	6873251629971269632		1a	126.0 ± 0.2	125.9 ± 0.2	0.17 ± 0.02	0.35 ± 0.07	2
‘OrbitalTargetedSearchValidated’	3176470817561155200		1a	17.4 ± 4e-3	17.4 ± 7e-3	0.23 ± 0.02	0.17 ± 0.05	2
‘OrbitalTargetedSearchValidated’	4552227182675443584		1a	10.2 ± 2e-4	10.2 ± 2e-3	0.02 ± 2e-3	0.01 ± 0.07	2
‘OrbitalTargetedSearchValidated’	6448639343335797888		1a	29.7 ± 7e-3	29.8 ± 5e-2	0.37 ± 0.02	0.28 ± 0.17	2
‘OrbitalTargetedSearchValidated’	5657709399107097600		1a	243.9 ± 0.9	243.8 ± 0.8	0.10 ± 0.03	0.14 ± 0.05	2
‘OrbitalTargetedSearchValidated’	4597154602175212672		1a	181.9 ± 0.3	183.9 ± 1.6	0.26 ± 0.02	0.11 ± 0.21	2
‘OrbitalTargetedSearchValidated’	1905308073023457920		1a	8.8 ± 1e-4	8.8 ± 5e-3	0.38 ± 4e-3	0.31 ± 0.10	2
‘OrbitalTargetedSearchValidated’	5547864407933928320		1a	993.0 ± 29.7	975.5 ± 28.3	0.43 ± 0.03	0.46 ± 0.02	2
‘OrbitalTargetedSearchValidated’	5961294592641279104		1a	765.1 ± 7.4	728.9 ± 10.3	0.08 ± 0.02	0.13 ± 0.04	2
‘OrbitalTargetedSearchValidated’	5220689364275188224		1a	226.2 ± 0.1	228.0 ± 1.4	0.38 ± 3e-3	0.40 ± 0.10	2
‘OrbitalTargetedSearchValidated’	797106798693569536		1a	611.8 ± 14.8	599.2 ± 0.4	0.34 ± 0.06	0.20 ± 4e-3	2
‘OrbitalTargetedSearchValidated’	6130370305216737408		1a	19.5 ± 3e-3	19.4 ± 2e-2	0.13 ± 0.02	8e-4 ± 0.21	2
‘OrbitalTargetedSearchValidated’	670216834655936128		1a	161.3 ± 0.4	161.1 ± 0.2	0.26 ± 0.03	0.32 ± 0.04	2
‘OrbitalTargetedSearchValidated’	1401541841225053696		1a	325.2 ± 1.2	325.7 ± 0.4	0.28 ± 0.01	0.30 ± 0.01	2
‘OrbitalTargetedSearchValidated’	5096613016130459136		1a	51.6 ± 4e-2	51.6 ± 0.1	0.24 ± 0.01	0.26 ± 0.09	2
‘OrbitalTargetedSearchValidated’	5503370333440752384		1a	815.4 ± 41.6	827.5 ± 37.3	0.10 ± 0.12	0.09 ± 0.13	2
‘OrbitalTargetedSearchValidated’	3703975672901804160		1a	56.5 ± 3e-2	56.2 ± 0.1	0.32 ± 0.01	0.24 ± 0.07	2
‘OrbitalTargetedSearchValidated’	596878550087942528		1a	10.2 ± 2e-4	10.2 ± 5e-3	0.02 ± 2e-3	0.37 ± 0.10	2
‘OrbitalTargetedSearchValidated’	4525943082344640256		1a	26.4 ± 8e-4	26.4 ± 6e-3	0.22 ± 3e-3	0.14 ± 0.03	2
‘OrbitalTargetedSearchValidated’	2431188610386566784		1a	879.3 ± 22.8	844.6 ± 19.9	0.16 ± 0.02	0.12 ± 0.04	2
‘OrbitalTargetedSearchValidated’	4253017049075877120		1a	21.0 ± 6e-3	21.0 ± 5e-2	0.01 ± 0.01	0.06 ± 0.31	2
‘OrbitalTargetedSearchValidated’	4921427313081081600		1a	1073.8 ± 50.3	1117.5 ± 168	0.12 ± 0.03	0.02 ± 0.05	2
‘OrbitalTargetedSearchValidated’	4254091856092504192		1a	52.8 ± 2e-2	52.6 ± 0.2	0.35 ± 0.02	0.17 ± 0.34	2
‘OrbitalTargetedSearchValidated’	603701328976020864		1a	44.1 ± 3e-2	44.3 ± 3e-2	0.30 ± 0.01	0.28 ± 0.07	2
‘OrbitalTargetedSearchValidated’	5065735499806985856		1a	125.0 ± 0.1	125.1 ± 0.1	0.56 ± 0.01	0.62 ± 0.08	2
‘OrbitalTargetedSearchValidated’	4556905020537693696		1a	641.1 ± 2.0	644.8 ± 0.9	0.25 ± 0.01	0.25 ± 0.01	2
‘OrbitalTargetedSearchValidated’	5361232754474635776		1a	815.6 ± 4.9	818.8 ± 42.0	0.31 ± 0.02	0.21 ± 0.08	2
‘OrbitalTargetedSearchValidated’	4544260465016425344		1a	235.7 ± 0.7	235.7 ± 0.6	0.49 ± 0.02	0.54 ± 0.06	2
‘OrbitalTargetedSearchValidated’	2633003866585490944		1a	494.3 ± 4.5	503.7 ± 9.1	0.06 ± 0.07	0.24 ± 0.11	2
‘OrbitalTargetedSearchValidated’	5997977839551049216		1a	225.2 ± 0.5	225.5 ± 0.2	0.32 ± 0.01	0.31 ± 0.01	2
‘OrbitalTargetedSearchValidated’	4902020348734646912		1a	189.7 ± 0.5	187.0 ± 3.6	0.06 ± 0.03	0.36 ± 0.38	2
‘OrbitalTargetedSearchValidated’	4824625656537163008		1a	81.1 ± 0.1	80.9 ± 0.1	0.43 ± 0.09	0.36 ± 0.05	2
‘OrbitalTargetedSearchValidated’	6525140510537736448		1a	11.6 ± 4e-4	11.6 ± 4e-4	0.18 ± 4e-3	0.30 ± 0.08	2
‘OrbitalTargetedSearchValidated’	4568198963458261632		1a	430.6 ± 0.7	433.7 ± 0.5	0.57 ± 0.02	0.54 ± 0.01	2
‘OrbitalTargetedSearchValidated’	3914521949074389632		1a	24.2 ± 2e-3	24.1 ± 4e-2	0.28 ± 0.01	0.15 ± 0.14	2
‘OrbitalTargetedSearchValidated’	4666680536328166528		1a	511.2 ± 2.2	515.8 ± 3.2	0.03 ± 0.03	0.11 ± 0.05	2
‘OrbitalTargetedSearchValidated’	3683727208499815936		1a	114.8 ± 0.1	115.3 ± 0.6	0.49 ± 0.03	0.47 ± 0.25	2
‘OrbitalTargetedSearchValidated’	283446302278774528		1a	22.8 ± 3e-3	22.8 ± 8e-3	0.32 ± 0.01	0.30 ± 0.04	2
‘OrbitalTargetedSearchValidated’	3064145014608187392		1a	115.1 ± 0.1	115.0 ± 0.1	0.36 ± 0.02	0.38 ± 0.02	2
‘OrbitalTargetedSearchValidated’	2185171578009765632	HD193468	1b [†]		291.8 ± 0.9		0.71 ± 0.06	1
‘OrbitalTargetedSearchValidated’	6678530491511225856		1b [†]		911.3 ± 2.9		0.49 ± 3e-3	2
‘OrbitalTargetedSearchValidated’	6778413151435607680		1b [†]		1010.2 ± 10.4		0.35 ± 0.01	2
‘OrbitalTargetedSearchValidated’	4748772376561143424	HIP13685	1b	1613.2 ± 178	1438.9 ± 132	0.68 ± 0.03	0.64 ± 0.03	1
‘OrbitalTargetedSearchValidated’	5865296850880144256		1b	989.1 ± 11.9	999.0 ± 11.8	0.09 ± 0.01	0.09 ± 0.01	2
‘OrbitalTargetedSearchValidated’	6511657371244871680		1b	1000.4 ± 7.0	990.6 ± 6.7	0.51 ± 4e-3	0.51 ± 4e-3	2
‘OrbitalTargetedSearchValidated’	1568219729458240128		1b	273.9 ± 0.1	273.8 ± 0.1	0.76 ± 4e-3	0.75 ± 3e-3	2
‘OrbitalTargetedSearchValidated’	4354357901908595456		1b	133.5 ± 0.1	133.4 ± 0.1	0.27 ± 0.01	0.24 ± 0.01	2
‘OrbitalTargetedSearchValidated’	1436561046051723648		1b	316.2 ± 0.6	316.1 ± 0.5	0.56 ± 0.02	0.54 ± 0.02	2
‘OrbitalTargetedSearchValidated’	2162250505790084480		1b	585.0 ± 1.0	584.3 ± 2.9	0.27 ± 0.01	0.25 ± 0.03	2
‘OrbitalTargetedSearchValidated’	1215279005201870336		1b	151.1 ± 0.2	150.5 ± 0.3	0.57 ± 0.01	0.52 ± 0.04	2
‘OrbitalTargetedSearchValidated’	5041087953805187584		1b	665.8 ± 2.1	665.6 ± 2.4	0.81 ± 0.01	0.78 ± 0.01	2
‘OrbitalTargetedSearchValidated’	5045853099761604096		1b	114.9 ± 0.1	115.0 ± 0.1	0.13 ± 0.01	0.20 ± 0.02	2
‘OrbitalTargetedSearchValidated’	1918953867019478144		1b	349.4 ± 1.0	347.3 ± 1.0	0.42 ± 0.03	0.44 ± 0.03	2
‘OrbitalTargetedSearchValidated’	787672026858725632		1b	330.6 ± 0.4	331.0 ± 0.2	0.59 ± 0.02	0.53 ± 0.01	2
‘OrbitalTargetedSearchValidated’	2843794470563210496		1b	145.3 ± 0.1	145.2 ± 0.1	0.47 ± 0.02	0.48 ± 0.01	2
‘OrbitalTargetedSearchValidated’	6075391292173461760		1b	786.9 ± 3.9	777.6 ± 10.5	0.11 ± 0.01	0.11 ± 0.02	2
‘OrbitalTargetedSearchValidated’	5289793360842855808		1b	690.8 ± 1.5	692.3 ± 1.5	0.07 ± 0.01	0.06 ± 0.01	2
‘OrbitalTargetedSearchValidated’	3028470161558479232		1b	121.4 ± 3e-2	121.4 ± 3e-2	0.09 ± 0.01	0.10 ± 0.01	2
‘OrbitalTargetedSearchValidated’	6708063202046601344		1b	120.0 ± 4e-2	119.9 ± 0.1	0.44 ± 0.01	0.39 ± 0.02	2
‘OrbitalTargetedSearchValidated’	2208365672715184256		1b	691.5 ± 2.7	696.5 ± 3.1	0.41 ± 0.01	0.43 ± 0.01	2
‘OrbitalTargetedSearchValidated’	5013703860801457280		1b	299.0 ± 1.2	297.8 ± 1.0	0.33 ± 0.05	0.19 ± 0.05	2
‘OrbitalTargetedSearchValidated’	2983397469077381632		1b	854.7 ± 3.3	865.6 ± 3.8	0.04 ± 4e-3	0.09 ± 0.01	2
‘OrbitalTargetedSearchValidated’	316256588242414592		1b	166.7 ± 0.2	167.7 ± 0.3	0.21 ± 0.02	0.10 ± 0.04	2
‘OrbitalTargetedSearchValidated’	6827751124390424320		1b	306.3 ± 0.3	306.2 ± 0.2	0.22 ± 0.01	0.24 ± 0.01	2
‘OrbitalTargetedSearchValidated’	3603119331007599232		1b	145.4 ± 0.1	145.5 ± 0.1	0.30 ± 0.01	0.28 ± 0.02	2
‘OrbitalTargetedSearchValidated’	6685418107226825216		1b	554.1 ± 0.9	554.0 ± 0.9	0.43 ± 0.02	0.40 ± 0.02	2
‘OrbitalTargetedSearchValidated’	5710296119685549440		1b	41.0 ± 1e-2	41.0 ± 2e-2	0.16 ± 0.01	0.15 ± 0.02	2
‘OrbitalTargetedSearchValidated’	4829273360906556672		1b	305.8 ± 1.9	310.7 ± 2.6	0.56 ± 0.04	0.48 ± 0.08	2
‘OrbitalTargetedSearchValidated’	4830490966955576960		1b	693.7 ± 2.7	694.0 ± 1.7	0.57 ± 0.02	0.53 ± 0.02	2
‘OrbitalTargetedSearchValidated’	4832672020067562624		1b	204.1 ± 0.1	204.1 ± 0.1	0.20 ± 0.01	0.16 ± 0.01	2

References. (1) Gaia DR3 table nss_two_body_orbit with nss_solution_type = (a) SB1, (b) AstroSpectroSB1, (c) SB2;

Notes. † : Gaia reference data used for validation was eventually not published in Gaia DR3, therefore no reference values are provided.

Table A.4. Gaia reference solution parameters for ‘OrbitalTargetedSearchValidated’ solutions, 2 of 2. See Appendix A for details.

nss_solution_type	Gaia DR3 source_id	Name	Ref.	Ref. P [d]	Our P [d]	Ref. e	Our e	M_c
‘OrbitalTargetedSearchValidated’	5841850590016284544		1b	1170.8 ± 14.1	1189.9 ± 12.6	0.42 ± 0.01	0.43 ± 0.01	2
‘OrbitalTargetedSearchValidated’	5306416671004618240		1b	513.7 ± 0.7	513.2 ± 0.6	0.40 ± 0.01	0.36 ± 0.01	2
‘OrbitalTargetedSearchValidated’	6345896578791113472		1b	170.8 ± 0.1	171.2 ± 0.1	0.37 ± 0.01	0.31 ± 0.03	2
‘OrbitalTargetedSearchValidated’	5645712490304616320		1b	864.3 ± 5.1	867.3 ± 6.0	0.11 ± 0.01	0.10 ± 0.01	2
‘OrbitalTargetedSearchValidated’	5523408692342861696		1b	685.4 ± 1.5	684.2 ± 2.3	0.02 ± 0.01	0.04 ± 0.02	2
‘OrbitalTargetedSearchValidated’	4949308041743808384		1b	821.1 ± 1.9	823.9 ± 2.0	0.28 ± 4e-3	0.29 ± 4e-3	2
‘OrbitalTargetedSearchValidated’	4800235533695856256		1b	430.6 ± 1.7	431.5 ± 1.6	0.13 ± 0.03	0.11 ± 0.03	2
‘OrbitalTargetedSearchValidated’	4950186203640554880		1b	305.5 ± 0.3	305.6 ± 0.3	0.17 ± 0.01	0.17 ± 5e-3	2
‘OrbitalTargetedSearchValidated’	6076629204819105664		1b	143.6 ± 0.1	143.9 ± 0.2	0.13 ± 0.01	0.24 ± 0.05	2
‘OrbitalTargetedSearchValidated’	2299519550340109696		1b	141.7 ± 4e-2	141.7 ± 0.1	0.31 ± 0.01	0.28 ± 0.02	2
‘OrbitalTargetedSearchValidated’	5629502218573747584		1b	108.8 ± 2e-2	108.7 ± 5e-2	0.08 ± 0.01	0.15 ± 0.02	2
‘OrbitalTargetedSearchValidated’	5459518648630576768		1b	274.6 ± 0.2	274.2 ± 0.3	0.16 ± 0.01	0.15 ± 0.01	2
‘OrbitalTargetedSearchValidated’	2888649013058936448		1b	1105.5 ± 22.0	1108.9 ± 41.9	0.41 ± 0.01	0.40 ± 0.02	2
‘OrbitalTargetedSearchValidated’	2889380085212270080		1b	1165.6 ± 30.4	1157.3 ± 23.1	0.24 ± 0.01	0.24 ± 0.01	2
‘OrbitalTargetedSearchValidated’	1527631807474248448		1b	709.9 ± 0.6	710.1 ± 0.6	0.31 ± 2e-3	0.31 ± 2e-3	2
‘OrbitalTargetedSearchValidated’	4529439851267809024		1b	196.6 ± 0.1	196.6 ± 5e-2	0.17 ± 0.01	0.17 ± 0.01	2
‘OrbitalTargetedSearchValidated’	3638745672411053952		1b	206.7 ± 0.2	206.7 ± 0.7	0.32 ± 0.01	0.33 ± 0.03	2
‘OrbitalTargetedSearchValidated’	6631710606341412096		1b	937.0 ± 6.4	933.3 ± 6.7	0.31 ± 0.01	0.31 ± 0.01	2
‘OrbitalTargetedSearchValidated’	5490419250399767680		1b	228.7 ± 0.2	228.2 ± 0.2	0.43 ± 0.01	0.48 ± 0.01	2
‘OrbitalTargetedSearchValidated’	3579784327012046336		1b	645.0 ± 0.9	648.7 ± 1.8	0.55 ± 5e-3	0.49 ± 0.02	2
‘OrbitalTargetedSearchValidated’	3116065985196889216		1b	852.4 ± 7.8	859.4 ± 7.8	0.46 ± 0.01	0.46 ± 0.01	2
‘OrbitalTargetedSearchValidated’	1294000704856807168		1b	125.3 ± 0.1	125.4 ± 0.1	0.28 ± 0.01	0.27 ± 0.01	2
‘OrbitalTargetedSearchValidated’	3569106488558337792		1b	212.3 ± 0.5	217.3 ± 0.1	0.23 ± 0.03	0.53 ± 0.02	2
‘OrbitalTargetedSearchValidated’	3579784327012046336		1b	90.1 ± 5e-2	90.0 ± 0.2	0.49 ± 0.01	0.43 ± 0.07	2
‘OrbitalTargetedSearchValidated’	861776842822330368		1b	33.6 ± 9e-3	33.6 ± 1e-2	0.19 ± 0.03	0.26 ± 0.04	2
‘OrbitalTargetedSearchValidated’	5545537291566200320		1b	835.8 ± 4.9	840.2 ± 5.6	0.67 ± 5e-3	0.68 ± 5e-3	2
‘OrbitalTargetedSearchValidated’	4810832695483445760		1b	270.3 ± 0.2	269.6 ± 0.7	0.36 ± 5e-3	0.27 ± 0.04	2
‘OrbitalTargetedSearchValidated’	48253703990915066880		1b	85.5 ± 0.1	85.2 ± 0.2	0.05 ± 0.03	0.08 ± 0.09	2
‘OrbitalTargetedSearchValidated’	6542137929509574144		1b	573.1 ± 1.1	572.4 ± 0.9	0.22 ± 0.01	0.22 ± 0.01	2
‘OrbitalTargetedSearchValidated’	1014542369909518976		1b	154.4 ± 0.2	154.1 ± 0.3	0.40 ± 0.03	0.48 ± 0.08	2
‘OrbitalTargetedSearchValidated’	1648950576156773760		1b	564.3 ± 1.2	564.5 ± 0.9	0.16 ± 0.02	0.16 ± 0.01	2
‘OrbitalTargetedSearchValidated’	107511930591409280		1b	208.1 ± 0.5	207.4 ± 0.5	0.28 ± 0.02	0.29 ± 0.03	2
‘OrbitalTargetedSearchValidated’	1484569984328261632		1b	577.0 ± 0.8	579.1 ± 1.3	0.41 ± 0.01	0.41 ± 0.01	2
‘OrbitalTargetedSearchValidated’	1695571110421334144		1b	450.2 ± 0.6	450.3 ± 0.6	0.33 ± 0.01	0.32 ± 0.01	2
‘OrbitalTargetedSearchValidated’	266076492460606592		1b	567.1 ± 1.7	566.9 ± 1.3	0.44 ± 0.02	0.44 ± 0.01	2
‘OrbitalTargetedSearchValidated’	1305309456826990464		1b	533.6 ± 0.5	534.2 ± 0.5	0.22 ± 4e-3	0.22 ± 4e-3	2
‘OrbitalTargetedSearchValidated’	5564490982239584768		1b	716.1 ± 4.3	720.5 ± 5.2	0.17 ± 0.01	0.16 ± 0.01	2
‘OrbitalTargetedSearchValidated’	2396173975404592512		1b	478.2 ± 2.1	478.4 ± 1.9	0.13 ± 0.03	0.14 ± 0.02	2
‘OrbitalTargetedSearchValidated’	6661911579416783616		1b	62.8 ± 2e-2	62.9 ± 3e-2	0.37 ± 0.01	0.47 ± 0.06	2
‘OrbitalTargetedSearchValidated’	4650689681594278272		1b	951.7 ± 11.0	945.0 ± 14.0	0.09 ± 0.01	0.08 ± 0.02	2
‘OrbitalTargetedSearchValidated’	1813985523437968256		1b	302.5 ± 0.5	302.7 ± 0.4	0.24 ± 0.01	0.24 ± 0.01	2
‘OrbitalTargetedSearchValidated’	6807019282894453504		1b	150.8 ± 0.1	150.6 ± 0.1	0.19 ± 0.02	0.23 ± 0.02	2
‘OrbitalTargetedSearchValidated’	477432822246003840		1b	163.7 ± 0.2	163.5 ± 1.3	0.01 ± 0.01	0.38 ± 0.14	2
‘OrbitalTargetedSearchValidated’	422886126401496064		1b	295.5 ± 0.1	295.5 ± 0.1	0.26 ± 3e-3	0.26 ± 3e-3	2
‘OrbitalTargetedSearchValidated’	1615450866336763904		1b	390.3 ± 0.2	390.5 ± 0.3	0.09 ± 0.01	0.07 ± 0.02	2
‘OrbitalTargetedSearchValidated’	286293109680203008		1b	393.7 ± 0.5	393.7 ± 0.4	0.25 ± 0.02	0.18 ± 0.01	2
‘OrbitalTargetedSearchValidated’	4963661822446609792		1b	512.6 ± 0.5	513.1 ± 0.5	0.86 ± 0.01	0.87 ± 0.01	2
‘OrbitalTargetedSearchValidated’	4133650458966620672		1b	211.6 ± 0.4	211.1 ± 0.4	0.52 ± 0.01	0.53 ± 0.02	2
‘OrbitalTargetedSearchValidated’	4972788662311608960		1b	115.2 ± 1e-2	115.3 ± 4e-2	0.37 ± 4e-3	0.37 ± 0.01	2
‘OrbitalTargetedSearchValidated’	5236430419447179776		1b	169.6 ± 0.1	169.6 ± 0.1	0.40 ± 0.01	0.40 ± 0.01	2
‘OrbitalTargetedSearchValidated’	4594158089392172928		1b	178.7 ± 0.3	178.3 ± 0.3	0.56 ± 0.02	0.57 ± 0.05	2
‘OrbitalTargetedSearchValidated’	1348238101626698368		1b	1253.5 ± 18.4	1253.7 ± 20.7	0.40 ± 0.01	0.40 ± 0.01	2
‘OrbitalTargetedSearchValidated’	5631222984331124864		1b	15.4 ± 2e-3	15.4 ± 2e-3	0.36 ± 0.02	0.29 ± 0.03	2
‘OrbitalTargetedSearchValidated’	6257172793656011520		1b	552.2 ± 1.9	555.5 ± 1.1	0.70 ± 0.02	0.63 ± 0.01	2
‘OrbitalTargetedSearchValidated’	5526720593166247680	HD72834	1c	145.3 ± 0.1	145.3 ± 0.2	0.68 ± 0.01	0.56 ± 0.03	1
‘OrbitalTargetedSearchValidated’	5583755078792642304	HD47391	1c	214.1 ± 0.1	210.3 ± 0.4	0.19 ± 4e-3	0.17 ± 0.04	1
‘OrbitalTargetedSearchValidated’	4321775627212956672	HD184962	1c	33.7 ± 4e-3	33.4 ± 0.1	0.27 ± 6e-3	0.31 ± 0.26	1
‘OrbitalTargetedSearchValidated’	6490284754986167552	GJ4331	1c	24.8 ± 3e-3	24.7 ± 2e-2	0.50 ± 7e-3	0.55 ± 0.21	1
‘OrbitalTargetedSearchValidated’	6158160019228728448	HD109524	1c	12.0 ± 1e-4	12.0 ± 6e-3	0.17 ± 2e-3	0.33 ± 0.13	1
‘OrbitalTargetedSearchValidated’	2035577729682322176		1c	18.8 ± 4e-4	18.8 ± 5e-3	0.31 ± 2e-3	0.30 ± 0.06	2
‘OrbitalTargetedSearchValidated’	1067685718250692352		1c	30.5 ± 6e-4	30.5 ± 1e-2	0.19 ± 1e-3	0.26 ± 0.05	2
‘OrbitalTargetedSearchValidated’	6017724140678769024		1c	31.8 ± 1e-3	31.9 ± 9e-3	0.15 ± 3e-3	0.22 ± 0.04	2
‘OrbitalTargetedSearchValidated’	5534280594604579584		1c	175.5 ± 0.1	176.7 ± 0.3	0.15 ± 0.01	0.20 ± 0.03	2

References. (1) Gaia DR3 table nss_two_body_orbit with nss_solution_type = (a) SB1, (b) AstroSpectroSB1, (c) SB2;

Appendix B: Examples of Gaia archive queries

This section describes Gaia archive queries in the ADQL format that return the various selections and tables presented in this paper. These queries can be made online in the *Gaia* archive at <https://gea.esac.esa.int/archive/>:

Appendix B.1: Sky source density and number of observations

Input data for HEALPix (Górski et al. 2002) plots of the source sky density and number of FoV observations in the lower two panels of Fig. 4:

```
select
  gaia_healpix_index(8, source_id) AS hpx8,
  round( count(*) / 0.052441, 0) as sources_per_sq_deg,
  round( avg(astrometric_matched_transits), 1) as mean_agis_fov,
  round( max(astrometric_matched_transits), 0) as max_agis_fov
from gaiadr3.gaia_source
group by hpx8
```

Appendix B.2: Flag counts

Counts of flags in `nss_two_body_orbit` for our `nss_solution_type`'s discussed in Sect. 3.3:

```
select
  flags,
  nss_solution_type,
  count(source_id) as counts
from gaiadr3.nss_two_body_orbit
where nss_solution_type in
  ('OrbitalTargetedSearch', 'OrbitalAlternative', 'OrbitalTargetedSearchValidated', 'OrbitalAlternativeValidated')
group by nss_solution_type, flags
order by flags, counts
```

Appendix B.3: Table 2 counts

Counts of `source_id`'s with alternative solutions in table `nss_two_body_orbit`:

```
select
  nss_solution_type_exopl,
  nonexopl.nss_solution_type as nss_solution_type_other,
  count(source_id) as counts from
  (
    select source_id, cnt.num_solutions, orb.nss_solution_type as nss_solution_type_exopl, period as period_exopl
    from gaiadr3.nss_two_body_orbit orb join
    ( select source_id, count(source_id) as num_solutions from gaiadr3.nss_two_body_orbit group by source_id
    ) as cnt using (source_id)
    where nss_solution_type in
      ('OrbitalTargetedSearch', 'OrbitalAlternative', 'OrbitalTargetedSearchValidated', 'OrbitalAlternativeValidated')
      and cnt.num_solutions = 2 -- subset of source_id with two entries (there are none with >2)
  ) as exopl
join gaiadr3.nss_two_body_orbit nonexopl using (source_id) where nonexopl.nss_solution_type not in
  ('OrbitalTargetedSearch', 'OrbitalAlternative', 'OrbitalTargetedSearchValidated', 'OrbitalAlternativeValidated')
group by nss_solution_type_exopl, nss_solution_type
order by nss_solution_type_exopl asc, counts desc
```

Counts of `source_id`'s with an alternative solution in table `nss_non_linear_spectro`:

```
select
  exopl.nss_solution_type as nss_solution_type_exopl,
  npls.nss_solution_type as nss_solution_type_other,
  count(source_id) as counts
from gaiadr3.nss_non_linear_spectro npls
join gaiadr3.nss_two_body_orbit exopl using (source_id) where exopl.nss_solution_type in
  ('OrbitalTargetedSearch', 'OrbitalAlternative', 'OrbitalTargetedSearchValidated', 'OrbitalAlternativeValidated')
group by exopl.nss_solution_type, npls.nss_solution_type
order by exopl.nss_solution_type asc, counts desc
```

Appendix C: Acronyms

Acronym	Description
ADQL	Astronomical Data Query Language
AL	ALong scan (direction)
AC	ACross scan (direction)
DACE	Data and Analysis Center for Exoplanets
DE-MCMC	Differential Evolution Markov Chain Monte Carlo
DPAC	Data Processing and Analysis Consortium
DR1	Gaia Data Release 1
DR2	Gaia Data Release 2
EDR3	Gaia Early Data Release 3
DR3	Gaia Data Release 3
GA	Genetic Algorithm
NSS	Non-Single Star

Appendix D: Gaia acknowledgements

This work presents results from the European Space Agency (ESA) space mission Gaia. Gaia data are being processed by the Gaia Data Processing and Analysis Consortium (DPAC). Funding for the DPAC is provided by national institutions, in particular the institutions participating in the Gaia MultiLateral Agreement (MLA). The Gaia mission website is <https://www.cosmos.esa.int/gaia>. The Gaia archive website is <https://archives.esac.esa.int/gaia>.

The Gaia mission and data processing have financially been supported by, in alphabetical order by country:

- the Algerian Centre de Recherche en Astronomie, Astrophysique et Géophysique of Bouzareah Observatory;
- the Austrian Fonds zur Förderung der wissenschaftlichen Forschung (FWF) Hertha Firnberg Programme through grants T359, P20046, and P23737;
- the BELgian federal Science Policy Office (BEL-SPO) through various PROgramme de Développement d’Expériences scientifiques (PRODEX) grants and the Polish Academy of Sciences - Fonds Wetenschappelijk Onderzoek through grant VS.091.16N, and the Fonds de la Recherche Scientifique (FNRS), and the Research Council of Katholieke Universiteit (KU) Leuven through grant C16/18/005 (Pushing AsteRoseismology to the next level with TESS, GaiA, and the Sloan DiGital Sky SurVEy – PARADISE);
- the Brazil-France exchange programmes Fundação de Amparo à Pesquisa do Estado de São Paulo (FAPESP) and Coordenação de Aperfeiçoamento de Pessoal de Nível Superior (CAPES) - Comité Français d’Evaluation de la Coopération Universitaire et Scientifique avec le Brésil (COFECUB);
- the Chilean Agencia Nacional de Investigación y Desarrollo (ANID) through Fondo Nacional de Desarrollo Científico y Tecnológico (FONDECYT) Regular Project 1210992 (L. Chemin);
- the National Natural Science Foundation of China (NSFC) through grants 11573054, 11703065, and 12173069, the China Scholarship Council through grant 201806040200, and the Natural Science Foundation of Shanghai through grant 21ZR1474100;
- the Tenure Track Pilot Programme of the Croatian Science Foundation and the École Polytechnique Fédérale de Lausanne and the project TTP-2018-07-1171 ‘Mining the Variable Sky’, with the funds of the Croatian-Swiss Research Programme;
- the Czech-Republic Ministry of Education, Youth, and Sports through grant LG 15010 and INTER-EXCELLENCE grant LTAUSA18093, and the Czech Space Office through ESA PECS contract 98058;
- the Danish Ministry of Science;
- the Estonian Ministry of Education and Research through grant IUT40-1;
- the European Commission’s Sixth Framework Programme through the European Leadership in Space Astrometry (ELSA) Marie Curie Research Training Network (MRTN-CT-2006-033481), through Marie Curie project PIOFGA-2009-255267 (Space AsteroSeismology & RR Lyrae stars, SAS-RRL), and through a Marie Curie Transfer-of-Knowledge (ToK) fellowship (MTKD-CT-2004-014188); the European Commission’s Seventh Framework Programme through grant FP7-606740 (FP7-SPACE-2013-1) for the Gaia European Network for Improved data User Services (GENIUS) and through grant 264895 for the Gaia Research for European Astronomy Training (GREAT-ITN) network;
- the European Cooperation in Science and Technology (COST) through COST Action CA18104 ‘Revealing the Milky Way with Gaia (MW-Gaia)’;
- the European Research Council (ERC) through grants 320360, 647208, and 834148 and through the European Union’s Horizon 2020 research and innovation and excellent science programmes through Marie Skłodowska-Curie grant 745617 (Our Galaxy at full HD – Gal-HD) and 895174 (The build-up and fate of self-gravitating systems in the Universe) as well as grants 687378 (Small Bodies: Near and Far), 682115 (Using the Magellanic Clouds to Understand the Interaction of Galaxies), 695099 (A sub-percent distance scale from binaries and Cepheids – CepBin), 716155 (Structured ACCREtion Disks – SACCRED), 951549 (Sub-percent calibration of the extragalactic distance scale in the era of big surveys – UniverScale), and 101004214 (Innovative Scientific Data Exploration and Exploitation Applications for Space Sciences – EXPLORE);
- the European Science Foundation (ESF), in the framework of the Gaia Research for European Astronomy Training Research Network Programme (GREAT-ESF);
- the European Space Agency (ESA) in the framework of the Gaia project, through the Plan for European Cooperating States (PECS) programme through contracts C98090 and 4000106398/12/NL/KML for Hungary, through contract 4000115263/15/NL/IB for Germany, and through PROgramme de Développement d’Expériences scientifiques (PRODEX) grant 4000127986 for Slovenia;
- the Academy of Finland through grants 299543, 307157, 325805, 328654, 336546, and 345115 and the Magnus Ehrnrooth Foundation;
- the French Centre National d’Études Spatiales (CNES), the Agence Nationale de la Recherche (ANR) through grant ANR-10-IDEX-0001-02 for the ‘Investissements d’avenir’ programme, through grant ANR-15-CE31-0007 for project ‘Modelling the Milky Way in the Gaia era’ (MOD4Gaia), through grant ANR-14-CE33-0014-01 for project ‘The Milky Way disc formation in the Gaia era’ (ARCHEOGAL), through grant ANR-15-CE31-0012-01 for project ‘Unlocking the potential of Cepheids as primary distance calibrators’ (UnlockCepheids), through grant ANR-19-CE31-0017 for project ‘Secular evolution of galxies’ (SEGAL), and through grant ANR-18-CE31-0006 for project ‘Galactic Dark Matter’ (GaDaMa), the Centre National de la Recherche Scientifique (CNRS) and its SNO Gaia of the Institut des Sciences de l’Univers (INSU), its Programmes Nationaux: Cosmologie et Galaxies (PNCG), Gravitation Références Astronomie Métrologie (PNGRAM), Planétologie (PNP), Physique et

- Chimie du Milieu Interstellaire (PCMI), and Physique Stellaire (PNPS), the ‘Action Fédératrice Gaia’ of the Observatoire de Paris, the Région de Franche-Comté, the Institut National Polytechnique (INP) and the Institut National de Physique nucléaire et de Physique des Particules (IN2P3) co-funded by CNES;
- the German Aerospace Agency (Deutsches Zentrum für Luft- und Raumfahrt e.V., DLR) through grants 50QG0501, 50QG0601, 50QG0602, 50QG0701, 50QG0901, 50QG1001, 50QG1101, 50QG1401, 50QG1402, 50QG1403, 50QG1404, 50QG1904, 50QG2101, 50QG2102, and 50QG2202, and the Centre for Information Services and High Performance Computing (ZIH) at the Technische Universität Dresden for generous allocations of computer time;
 - the Hungarian Academy of Sciences through the Lendület Programme grants LP2014-17 and LP2018-7 and the Hungarian National Research, Development, and Innovation Office (NKFIH) through grant KKP-137523 (‘SeismoLab’);
 - the Science Foundation Ireland (SFI) through a Royal Society - SFI University Research Fellowship (M. Fraser);
 - the Israel Ministry of Science and Technology through grant 3-18143 and the Tel Aviv University Center for Artificial Intelligence and Data Science (TAD) through a grant;
 - the Agenzia Spaziale Italiana (ASI) through contracts I/037/08/0, I/058/10/0, 2014-025-R.0, 2014-025-R.1.2015, and 2018-24-HH.0 to the Italian Istituto Nazionale di Astrofisica (INAF), contract 2014-049-R.0/1/2 to INAF for the Space Science Data Centre (SSDC, formerly known as the ASI Science Data Center, ASDC), contracts I/008/10/0, 2013/030/I.0, 2013-030-I.0.1-2015, and 2016-17-I.0 to the Aerospace Logistics Technology Engineering Company (ALTEC S.p.A.), INAF, and the Italian Ministry of Education, University, and Research (Ministero dell’Istruzione, dell’Università e della Ricerca) through the Premiale project ‘Mining The Cosmos Big Data and Innovative Italian Technology for Frontier Astrophysics and Cosmology’ (MITiC);
 - the Netherlands Organisation for Scientific Research (NWO) through grant NWO-M-614.061.414, through a VICI grant (A. Helmi), and through a Spinoza prize (A. Helmi), and the Netherlands Research School for Astronomy (NOVA);
 - the Polish National Science Centre through HARMONIA grant 2018/30/M/ST9/00311 and DAINA grant 2017/27/L/ST9/03221 and the Ministry of Science and Higher Education (MNiSW) through grant DIR/WK/2018/12;
 - the Portuguese Fundação para a Ciência e a Tecnologia (FCT) through national funds, grants SFRH/BD/128840/2017 and PTDC/FIS-AST/30389/2017, and work contract DL 57/2016/CP1364/CT0006, the Fundo Europeu de Desenvolvimento Regional (FEDER) through grant POCI-01-0145-FEDER-030389 and its Programa Operacional Competitividade e Internacionalização (COMPETE2020) through grants UIDB/04434/2020 and UIDP/04434/2020, and the Strategic Programme UIDB/00099/2020 for the Centro de Astrofísica e Gravitação (CENTRA);
 - the Slovenian Research Agency through grant P1-0188;
 - the Spanish Ministry of Economy (MINECO/FEDER, UE), the Spanish Ministry of Science and Innovation (MICIN), the Spanish Ministry of Education, Culture, and Sports, and the Spanish Government through grants BES-2016-078499, BES-2017-083126, BES-C-2017-0085, ESP2016-80079-C2-1-R, ESP2016-80079-C2-2-R, FPU16/03827, PDC2021-121059-C22, RTI2018-095076-B-C22, and TIN2015-65316-P (‘Computación de Altas Prestaciones VII’), the Juan de la Cierva Incorporación Programme (FJCI-2015-2671 and IJC2019-04862-I for F. Anders), the Severo Ochoa Centre of Excellence Programme (SEV2015-0493), and MICIN/AEI/10.13039/501100011033 (and the European Union through European Regional Development Fund ‘A way of making Europe’) through grant RTI2018-095076-B-C21, the Institute of Cosmos Sciences University of Barcelona (ICCUB, Unidad de Excelencia ‘María de Maeztu’) through grant CEX2019-000918-M, the University of Barcelona’s official doctoral programme for the development of an R+D+i project through an Ajuts de Personal Investigador en Formació (APIF) grant, the Spanish Virtual Observatory through project AyA2017-84089, the Galician Regional Government, Xunta de Galicia, through grants ED431B-2021/36, ED481A-2019/155, and ED481A-2021/296, the Centro de Investigación en Tecnologías de la Información y las Comunicaciones (CITIC), funded by the Xunta de Galicia and the European Union (European Regional Development Fund – Galicia 2014-2020 Programme), through grant ED431G-2019/01, the Red Española de Supercomputación (RES) computer resources at MareNostrum, the Barcelona Supercomputing Centre - Centro Nacional de Supercomputación (BSC-CNS) through activities AECT-2017-2-0002, AECT-2017-3-0006, AECT-2018-1-0017, AECT-2018-2-0013, AECT-2018-3-0011, AECT-2019-1-0010, AECT-2019-2-0014, AECT-2019-3-0003, AECT-2020-1-0004, and DATA-2020-1-0010, the Departament d’Innovació, Universitats i Empresa de la Generalitat de Catalunya through grant 2014-SGR-1051 for project ‘Models de Programació i Entorns d’Execució Paralels’ (MPEXPAN), and Ramon y Cajal Fellowship RYC2018-025968-I funded by MICIN/AEI/10.13039/501100011033 and the European Science Foundation (‘Investing in your future’);
 - the Swedish National Space Agency (SNSA/Rymdstyrelsen);
 - the Swiss State Secretariat for Education, Research, and Innovation through the Swiss Activités Nationales Complémentaires and the Swiss National Science Foundation through an Eccellenza Professorial Fellowship (award PCEFP2_194638 for R. Anderson);
 - the United Kingdom Particle Physics and Astronomy Research Council (PPARC), the United Kingdom Science and Technology Facilities Council (STFC), and the United Kingdom Space Agency (UKSA) through the following grants to the University of Bristol, the University of Cambridge, the University of Edinburgh, the University of Leicester, the Mullard Space Sciences Laboratory of University College London, and the United Kingdom Rutherford Appleton Laboratory (RAL): PP/D006511/1, PP/D006546/1, PP/D006570/1, ST/I000852/1, ST/J005045/1, ST/K00056X/1, ST/K000209/1, ST/K000756/1, ST/L006561/1, ST/N000595/1, ST/N000641/1, ST/N000978/1, ST/N001117/1, ST/S000089/1, ST/S000976/1, ST/S000984/1, ST/S001123/1, ST/S001948/1, ST/S001980/1, ST/S002103/1, ST/V000969/1, ST/W002469/1, ST/W002493/1, ST/W002671/1, ST/W002809/1, and EP/V520342/1.
- The GBOT programme uses observations collected at (i) the European Organisation for Astronomical Research in the Southern Hemisphere (ESO) with the VLT Survey Telescope (VST),

under ESO programmes 092.B-0165, 093.B-0236, 094.B-0181, 095.B-0046, 096.B-0162, 097.B-0304, 098.B-0030, 099.B-0034, 0100.B-0131, 0101.B-0156, 0102.B-0174, and 0103.B-0165; and (ii) the Liverpool Telescope, which is operated on the island of La Palma by Liverpool John Moores University in the Spanish Observatorio del Roque de los Muchachos of the Instituto de Astrofísica de Canarias with financial support from the United Kingdom Science and Technology Facilities Council, and (iii) telescopes of the Las Cumbres Observatory Global Telescope Network.